A New Approach to Sub-grid Surface Tension for LES of Two-phase Flows

W. Aniszewski[a,*], A. Bogusławski[b], M. Marek[b], A. Tyliszczak[b]

[a] *CNRS UMR 6614 - CORIA Rouen, Site Universitaire du Madrillet, Saint Etienne du Rouvray, France*
[b] *Institute of Thermal Machinery, Czestochowa University of Technology, Czestochowa, Poland*

arXiv:1404.7072v1 [physics.comp-ph] 28 Apr 2014

Abstract

In two-phase flow, the presence of inter-phasal surface – the interface – causes additional terms to appear in LES formulation. Those terms were ignored in contemporary works, for the lack of model and because the authors expected them to be of negligible influence. However, it has been recently shown by *a priori* DNS simulations that the negligibility assumption can be challenged. In the present work, a model for one of the sub-grid two-phase specific terms is proposed, using deconvolution of the velocity field and advection of the interface using that field. Using the model, the term can be included into LES. A brief presentation of the model is followed by numerical tests that assess the model's performance by comparison with *a priori* DNS results.

Keywords: two-phase flow, Large Eddy Simulation, surface tension, CLSVOF

1. Introduction

It is our focus in this work to present an algorithm that allows for calculation of sub-grid surface tension term that appears in Navier – Stokes equations within Large Eddy Simulation (LES) formulation when two-phase flow is considered. To make the required calculations, an entire numerical setup involving a solver, two-phase flow modules and a sub-grid model have been prepared. In the article solving Navier – Stokes equations, the Volume of Fluid (VOF) method and the Level Set (LS) method will be described only in minimum, providing the reader with necessary literature, while the focus is on the implementation of the Coupled Level Set and Volume of Fluid method and the ADM-τ model of sub-grid surface tension, which we describe in most detailed manner. Similarly, the introduction is focused solely on reviewing Large Eddy Simulation of two-phase flow and not two-phase flows in general.

Until the 1990s, simulations of turbulent flows involved mainly one-phase (gaseous) flows; behaviour of second phase was, e.g. in work of Elghobashi (1984) [16], calculated using discrete particles (undeformable and much smaller than mesh size) so that their concentrations could be predicted [16]. Similar work was published by Eaton in 1994 [15].

Explicit interface modelling using methods such as VOF was not applied in LES until the 2000s. Conference paper of Alajbegovic gave first accounts of applying Large Eddy Simulations to multiphase flow [2], where he even proposed a closure for sub-grid scale surface tension, but results were criticized as being weakly documented [47], and having little connection with changes of the interface topology [32]. In 2000s, many authors used standard LES implementations together with VOF two-phase advection scheme. Such approach uses filtered (large-scale, resolved) velocity field in which advection, traced by VOF or similar method takes place, and all specific sub-grid terms resulting from the presence of the interface are ignored [35]. In [31], Lakehal performed LES using Germano's dynamic procedure of bubbly shear flow and investigated bilateral dependence between turbulence parameters and bubbly phase. Klein & Janicka [29] simulated film breakup, and in 2004 a SAE paper of de Villers et al. [12] gave account of a jet breakup simulated with quasi-realistic conditions (with Reynolds number equal to 15000), including an investigation of resolved droplet distributions. Similar simulation in 2007 by Bianchi et al. [7] included more realistic generation of inlet conditions, turbulence spectrum analysis, finer grid and more realistic density ratio, with a little lower Reynolds numbers. Still, interface-specific sub-grid contributions were not accounted for. Similar in character was the work of Menard [38], in which authors used CLSVOF technique to track the interface. It is important to stress that the authors of [38, 7, 12] all performed simulations in 3D, that were rather time-consuming (between one [12] and several [38] months) despite being LES calculations. Many useful information about ligament formation, creation of larger droplets and their secondary breakup were thereby made available, however, care is advised in interpretation of such results as some of small scale structures "cannot be trusted" [13].

We will now turn to works that directly precede some of the results presented in this paper. Articles by Labourasse et al. [30], Vincent et al. [55], Toutant et al. [58] and

*Corresponding Author. email: aniszewski@coria.fr; tel. +33 (0)2 32 95 36 73, CNRS-UMR6614 CORIA, Universite de Rouen, Site Universitaire du Madrillet - BP 12, 76801 Saint Etienne du Rouvray cedex

Larocque et al. [33], appearing between 2006 and 2010 were centered around careful examination of all sub-grid terms that appear in a two or multi-phase flow as a result of spatial filtering. Work by Trontin et al. [21] focused on creating a data base for development of two-phase SGS models by performing DNS of bubbly flow, including the question of subgrid contribution into the turbulent kinetic energy budget. Labourasse et al. [30] presented wide mathematical background for LES of two-phase flow, and defined respective tensors, among which τ_{rnn}, the tensor connected with unresolved surface tension force, is modelled by present authors. All four articles were similar in concept, in that they were *a priori* evaluations of LES subgrid terms basing on DNS simulations. For example, [55] includes a phase-inversion problem similar to Rayleigh-Taylor instability, while [58] performs a simulation of a fluid droplet immersed in quasi-turbulent flow, similar in principle to Marek & Tyliszczak [37]. In all these cases, time evolution of all sub-grid tensors is investigated and magnitude of their components presented and classified in various ways – so that it constitutes a valuable material for LES calculations. None of these works proposes any model yet.

2. Description of the Flow

We consider the one-fluid formulation for the incompressible two-phase flow [4, 30, 59]

$$\frac{\partial \mathbf{u}}{\partial t} + \nabla \cdot \mathbf{u} \otimes \mathbf{u} = \frac{1}{\rho} \left(\nabla \cdot (-p\mathbf{I} + \mu \mathbf{D}) + \sigma \kappa \mathbf{n} \delta_S \right) + \mathbf{f}_g, \quad (1)$$

with continuity equation

$$\nabla \cdot \mathbf{u} = 0. \quad (2)$$

In (1), symbol $\mathbf{D}$ is used for rate of strain tensor

$$\mathbf{D} = \nabla \mathbf{u} + \nabla^T \mathbf{u},$$

while standard symbols $\mathbf{u}, p, \mu, \kappa$ and $\mathbf{n}$ are used respectively for velocity field, pressure, viscosity, interface curvature and interface normals. The $\mathbf{f}_g$ symbol stands for external (body) force such as gravity, while δ_S is the Dirac delta centered on the interface. The $\sigma\kappa\mathbf{n}\delta_S$ is denoted $\mathbf{f}_s$, by some authors [3, 59], and may be perceived as a surface tension force, which is of singular character, in that it is centered on the interface. The one-fluid formulation [28] is derived from formulations separate for every phase, such as (for k phases)

$$\frac{\partial \mathbf{u}^k}{\partial t} + \nabla \cdot \mathbf{u}^k \otimes \mathbf{u}^k = \frac{1}{\rho^k} \nabla \cdot \left(-p^k \mathbf{I} + \mu^k \mathbf{D}^k \right) + \mathbf{f}_g \quad (3)$$

and

$$\nabla \cdot \mathbf{u}^k = 0 \quad (4)$$

with appropriate jump conditions applied on the interface, from which the $\mathbf{f}_s$ term of (1) originates. In short, the jump conditions for incompressible flow with constant surface tension coefficient require jump conditions in the following form:

$$\mathbf{u}^1 = \mathbf{u}^2 \quad (5)$$

as the continuity condition over the interface between phases 1 and 2, and

$$[-p + 2\mu \mathbf{n} \cdot \mathbf{D} \cdot \mathbf{n}]_s = \sigma\kappa \quad (6)$$

for Navier – Stokes equation. In (6) we use the jump notation $[x]_s = x^1 - x^2$.

Paper by Labourasse [30], excellent coverage by Tryggvasson, Scardovelli and Zaleski [59] or one of present authors' PhD thesis [3] give broad specification of jump conditions and one-fluid formulation for two-phase flow.

If we denote subdomains $\Omega_1, \Omega_2 \subset \Omega$ as occupied by first and second phase, it needs to be noted that interfacial surface S may be introduced as a jump surface of one of the phases' characteristic function, for example

$$\chi^1(\mathbf{x}) = \begin{cases} 1 & \Leftrightarrow \mathbf{x} \in \Omega^1 \\ 0 & \Leftrightarrow \mathbf{x} \notin \Omega^1 \vee x \in S, \end{cases} \quad (7)$$

where Ω^1 is a subdomain occupied by phase 1. Obviously, for two-phase flow we have $\chi^2 = 1 - \chi^1$. In such a situation, additional equation has to be formally considered with (1) and (2), namely transport of the phase indicator function, that is

$$\frac{D\chi^1}{Dt} = 0. \quad (8)$$

3. Numerical Approach

3.1. Large Eddy Simulation - Single-phase Flow

The Large Eddy Simulation (LES) [48, 42] bases conceptually upon *spatial* filtering. Filtering is here defined as convolution with a chosen filter kernel. In one dimension

$$\overline{u(x)} = \int G(x - x') \mathbf{u}(x', t) dx' \ \wedge \ \int_{-\infty}^{\infty} G(x) dx = 1, \quad (9)$$

where G is the filter kernel. Multidimensional filtering is realized by a superposition of filters defined along three coordinate axes.

The $G(x)$ is either only locally nonzero in physical space of $x \in \mathbb{R}$ or defined in the spectral space to filter out large wave numbers, i.e. its Fourier transform is zero almost everywhere.

When single-phase flow is considered, the filtered Navier – Stokes equations become:

$$\frac{\partial \overline{\mathbf{u}}}{\partial t} + \nabla \cdot \underbrace{\overline{\mathbf{u} \otimes \mathbf{u}}}_{I} = \frac{1}{\rho} \nabla \cdot \left(-\overline{p} + \mu \overline{\mathbf{D}} \right) + \mathbf{f}_g \tag{10}$$

with continuity equation for filtered velocity:

$$\nabla \cdot \overline{\mathbf{u}} = 0. \tag{11}$$

From the definition (9), and examples of filters given below, it is clear that filtering is a linear operation; additionally, in (10) commutation of filtering and differentiation is assumed. In LES, by principle, only filtered variables are known, so $\mathbf{u}$ field is unknown. Because of this, term I in (10) cannot be directly calculated and has to be closed, that is, expressed using only $\overline{\mathbf{u}}$. A symbol τ_{luu} is introduced in [30] for this term, which is called sub-grid stress tensor. It has the following form:

$$\tau_{luu} = \left(\overline{\mathbf{u} \otimes \mathbf{u}} - \overline{\mathbf{u}} \otimes \overline{\mathbf{u}} \right), \tag{12}$$

which, substituted in (10) yields

$$\frac{\partial \overline{\mathbf{u}}}{\partial t} + \nabla \cdot \left(\overline{\mathbf{u}} \otimes \overline{\mathbf{u}} + \tau_{luu} \right) = \frac{1}{\rho} \nabla \cdot \left(-\overline{p} + \mu \overline{\mathbf{D}} \right) + \mathbf{f}_g \tag{13}$$

As it involves unknown non-filtered velocity field, number of closures exist for τ_{luu}.

3.2. Two-phase Flow

In two-phase flow, as we remember by comparing respective forms of N-S equations (10) and (1), at least one new term appears due to the presence of the surface tension force, that resulted from jump conditions being applied on the interface. The term is

$$\mathbf{f}_s = \sigma \kappa \mathbf{n} \delta_S \tag{14}$$

and it undergoes filtering similarly to one-phase specific terms. Alternatively, as mentioned by Labourasse et al. [30], it is possible to perform the filtering on the left hand side of jump conditions (6). In fact, [30] proposes considering (6) even in its more general form; thus, instead of considering $\overline{\mathbf{f}_s}$ we would be considering the term

$$\sum_k \overline{(\rho^k \mathbf{u}^k \otimes (\mathbf{u_s} - \mathbf{u}^k) - p^k \mathbf{I} + \mathbf{T}^k) \cdot \mathbf{n}^k \delta_S},$$

where $\mathbf{u}_s$ is the velocity of the interface. This strategy leads to severe complications, that is the need for closure not only for classical sub-grid term τ_{luu} but also amounts to formulating an approximate jump condition through the interface, therefore it is avoided [30, 55, 58]. In this article, we thus adhere to the simpler approach, that is the filtering of (14), as described below.

When considering surface-specific sub-grid (filtered) terms, Labourasse [30] notes also that in general, filtering might not commute with surface differentiation[1], that is the use of operator ∇_s. This is a remark similar in nature to aforementioned issue of commutation between filtering and ∇. In our work, we do not introduce any corrections connected to this possible lack of commutability, since $\nabla \cdot \mathbf{n} = \nabla_s \cdot \mathbf{n}$ provided that $\mathbf{n}$ extends off the interface [59]. Hence, we will not introduce any new differentiation operators (in [30], new operator $\widehat{\nabla_s}$ is introduced in this context).

When jump-conditions are introduced, phase-indicator functions χ^k, (7) are defined. These functions are filtered as well, as they are represented in any two-phase flow computation for example by levelset functions $\phi(x)$. They undergo advection under $\overline{\mathbf{u}}$ velocity field described by equation

$$\frac{D\chi^k}{Dt} = 0, \tag{15}$$

which is non-linear and due to filtering requires a closure. In contemporary literature this closure is ignored [58, 55]. In the present work, while still not presenting any closure for this term (which we decided to call "Sub-Grid Mass Transfer/Transport", SMT), we give short remarks concerning it below.

Formal filtering of $\mathbf{f}_s$ should take the form

$$\begin{aligned} \overline{\mathbf{f}_s} &= \int_\Omega G(\mathbf{x}, \Delta) \mathbf{f}_s(\mathbf{x}) d\mathbf{x} \\ &= \sigma \int_\Omega G(\mathbf{x}, \Delta) \left[(\nabla_s \cdot \mathbf{n}(x)) \mathbf{n}(x) \delta_S \right] dx \qquad (16) \\ &= \overline{(\nabla_s \cdot \mathbf{n}) \mathbf{n} \delta_S}, \qquad (17) \end{aligned}$$

which is not computable, since $\mathbf{n}$ is unknown in LES in favor of $\overline{\mathbf{n}}$. Thus, analogically to definition of τ_{luu}, the τ_{rnn} tensor is defined by

$$\tau_{rnn} = \sigma \left(\overline{\mathbf{n} \nabla_s \cdot \mathbf{n} \delta_S} - \overline{\mathbf{n}} \nabla_s \cdot \overline{\mathbf{n}} \right). \tag{18}$$

Constant surface tension σ is assumed. The τ_{rnn} is clearly a vector force, and will be nonzero only on the interface S. Introduction of τ_{rnn} into (13) results in

$$\begin{aligned} \frac{\partial \overline{\mathbf{u}}}{\partial t} + \nabla \cdot \left(\overline{\mathbf{u}} \otimes \overline{\mathbf{u}} + \tau_{luu} \right) &= \\ \frac{1}{\rho} \nabla \cdot \left(-\overline{p} + \mu \overline{\mathbf{D}} + \sigma \overline{\mathbf{n}} \nabla_s \cdot \overline{\mathbf{n}} + \tau_{rnn} \right) + \mathbf{f}_g, \qquad (19) \end{aligned}$$

which serves as a LES-specific form of Navier – Stokes equations applied for all calculations presented in this article.

To summarize, we may say that two-phase LES is characterized by emergence of number of tensors resulting from nonlinearity of filtered variables. First is the τ_{luu} sub-grid stress tensor. Second is the term connected with phase-indicator transfer (SMT), and is created by filtering of the phase-indicator advection equation. Finally, the sub-grid curvature tensor τ_{rnn} which has been formulated above.

[1] Although no numerical investigations pertaining to this issue exist at the moment.

4. Solving Navier – Stokes Equations

Applied Navier – Stokes solver was SAILOR-LES [61, 60, 49] , a projection-based high order code, utilizing a pseudo-spectral and 4th order compact discretisations for spatial, and low-storage Runge-Kutta schemes for temporal discretisation. LES approach has been applied using Smagorinsky sub-grid model for the τ_{luu} tensor in the oil-water mixing case described below[2]. To advance the interface, the CLSVOF method has been applied, as described e.g. by Sussman [53] or Menard [38]. Ghost-Fluid (GFM) technique [22] is used to couple the CLSVOF two-phase module with the solver. To facilitate calculations of two-phase flows, the SAILOR-LES solver includes the Multigrid [9] and the BiConjugate Gradients [23] techniques to solve the Poisson equation.

5. Advancing the Interface

The CLSVOF [53, 56, 57] method is based upon simultaneous advection of the interface using VOF and LS methods, which allows for corrections of the Level-Set distance function using VOF distribution. It allows for substantial improvement in traced mass' conservation over 'pure' LS methods [38], also its accuracy concerning surface tension calculation it is comparable with modern VOF approaches [43] and has been applied to cases such as bubble growth [51, 56] or jet atomisation [38].

In this section, the description of VOF and LS methods is shortened to a minimum, while CLSVOF is described in a detailed way; this is because our implementations of VOF and LS methods are standard, while certain differences may be found between our implementation of CLSVOF and published works [53, 51].

5.1. Level Set Method

The method is based upon the Level-Set function ϕ, which is equal in every point $\mathbf{x}$ to the minimum distance d between $\mathbf{x}$ and the interface S, so $\phi := d(\mathbf{x}, S)$. The function ϕ is therefore a *distance function*. The function is advected using the fact that its material derivative must vanish:

$$\frac{D\phi}{Dt} = \frac{\partial \phi(\mathbf{x},t)}{\partial t} + \mathbf{u}(\mathbf{x},t)\nabla\cdot\phi(\mathbf{x},t) = 0. \qquad (20)$$

It is assumed, that the traced interface is the zero-level of the ϕ function. Note that it means that we have an *implicit* interface representation, as the actual localization of zero-level set is not necessary to solve the advection equation. In Level-Set methods [34, 18, 17, 52], this equation can be solved directly, provided that accurate discretisation is used (ENO and WENO [39] schemes have been proposed in this context and WENO has been implemented in our code). During the advection, due to numerical errors, ϕ will in general lose its distance property. Therefore it must be reinitialized, which requires solving the redistancing equation

$$\frac{\partial \phi}{\partial t'} + \mathrm{sgn}(\phi_0)(|\nabla\phi| - 1) = 0, \qquad (21)$$

every few timesteps. In (21), t' is an internal re-initialization pseudo-timescale, and ϕ_0 is the function distribution before the reinitialisation.

Both advection and reinitialisation are known to cause changes in interface shape. Especially reinitialisation is known to cause smoothing of the ϕ distribution, which in computational practice may cause significant mass loss, especially when following small droplets or thin films [18].

In our implementation, the curvature is calculated directly from the level set by means of second order central differencing.

5.2. The Volume of Fluid Method

The Volume of Fluid (VOF) method is one of the best established methods for two-phase flows [26, 46, 59]. The method is built upon a conception of a control volume (grid cell) containing the traced fluid, with the quantity of fluid being expressed as an integral of traced fluid's characteristic function

$$C_{i,j} = \frac{1}{h^2}\int\limits_V \chi(x,y)dxdy,\ (x,y)\in(i,j), \qquad (22)$$

and called the *fraction function*. In here, we consider a two-dimensional example. This fraction function is discontinuous, and therefore direct solving of its advection equation is not feasible, as it leads to diffusion of the interface shape.

The discretized form of the advection equation for fraction function reads

$$h^2\frac{\partial C_{ij}(t)}{\partial t} + \int\limits_\Gamma \mathbf{u}\cdot\mathbf{n}\chi(\mathbf{x},t)d\Gamma = 0. \qquad (23)$$

If we denote as $F_{i+1/2,j}$ the amount of χ leaving the cell during Δt time step through the right wall[3] we can discretize (23) in time arriving at

$$\begin{aligned} C_{i,j}^{n+1} &= C_{i,j}^n + \frac{\Delta t}{\Delta x}\left(F_{i-1/2,j}^n - F_{i+1/2,j}^n\right) \\ &\quad + \frac{\Delta t}{\Delta y}\left(G_{i,j-1/2}^n - G_{i,j+1/2}^n\right), \end{aligned} \qquad (24)$$

[2] The choice of this sub-grid model (the simplest of many implemented within the code) is motivated by the fact that the sub-grid stress tensor τ_{luu} was not the subject of our main interests in this paper, nor was it measured for comparison. Instead, the modelled τ_{rnn} tensor has been compared with resolved inertial terms, as will be discussed below.

[3] Analogically $F_{i-1/2}$ is left wall flux, while $G_{i,j-1/2}$ and $G_{i,j+1/2}$ are respectively bottom and upper wall fluxes in y.

where $\Delta x = \Delta y = h$ and h is the grid spacing in uniform discretization. The fluxes formula above is derived from (23) by using also continuity equation (2). Obviously, when (24) is rewritten for 3D simulation, an additional term appears for the front and back wall fluxes. In modern implementation of VOF method, the F quantities (fluxes) are found geometrically, by the so-called interface reconstruction [46, 64, 41]. This reconstruction is demanding for the programmer, especially in 3D, however it has become a contemporary standard, since it guarantees perfect mass conservation. In our code, full implementation of VOF including PLIC (Piecewise Linear Interface Calculation) reconstruction of the interface has been performed.

The outgoing flux $F_{i,j,k}$ is an intersection of volume $u_{i+1/2,j,k}\Delta t\Delta y\Delta z$ containing right-hand side wall of cell[4], and geometrically represented volume C_{ijk} confined under the interface $\{\mathbf{n}_{i,j,k}, \alpha_{i,j,k}\}$. In actual implementation, calculation of the flux volume (or area, in two-dimensional case) requires considering all possible interface positions and matching appropriate formulae for volume/area. However, this is considerably simplified when one notices that in every case, the area confined between the interface

$$\{\mathbf{n}_{i,j,k}, \alpha_{i,j,k}\}$$

and the origin of the local coordinate set is always an intersection of a properly defined tetrahedron and the cell cube [59]. The procedures utilizing this observation have been described by Scardovelli & Zaleski [44] for rectangular grids. Note that for a given interface position $\{\mathbf{n}_{i,j,k}, \alpha_{i,j,k}\}$, one is now able to establish a 1: 1 functional dependence with the traced phase volume contained within the cell. So, when we fix the normal vector, we get

$$V = V(\alpha) \tag{25}$$

functional dependence, whose properties are discussed in [44, 59, 3] (this function can be reversed, to form $\alpha = \alpha(V) = \alpha(C_{ijk})$, which is essential for interface reconstruction in modern PLIC approach). Also, we emphasize that finding flux volumes for equation (24) is realized by using (25) with transformations of local coordinates within the cell.

As it will be mentioned below, (25) is employed within our CLSVOF implementation.

5.3. Implementation of the CLSVOF algorithm

CLSVOF algorithm is relatively complicated, and is usually [53] explained using numbered lists of algorithm steps. In here, we describe our implementation in a detailed way, together with a diagram of the basic method steps. In our approach, interaction between VOF and LS interface representations starts with generating an initial LS distribution, we then proceed along the stages described below.

[4]Provided that $u_{i+1/2,j,k}$ is positive, see [3, 59, 44] for details.

5.3.1. Comparing Level Set and VoF Interfaces

As it is evidenced by diagram in Fig. 1 which should be read starting from upper left corner, the algorithm starts with ϕ^n being a level set from previous time step (obviously, $n = 0$ at the code initialization). Then, as in 'pure' LS method, ϕ^n is advected with timestep dt, thus procuring a ϕ^{n+1}_{temp} distribution (IIa on Fig. 1). This is nothing else than ϕ^{n+1} one would obtain in pure LS method, yet in CLSVOF it is subject to further operations, hence the subscript. In order to enable juxtaposition of ϕ^{n+1}_{temp} with the effect of VOF advection, we first need to generate a (volume) fraction function C^n from initial level set ϕ^n. This is done (step I) using a dedicated function.

Let us define a function

$$\Psi\colon \mathbb{R}^\gamma \mapsto \mathbb{R}^\gamma, \tag{26}$$

(where γ stands for the dimension[5]) such that

$$\Psi(\phi_{ij}) = C_{ij}. \tag{27}$$

Thus, Ψ will be a function we need to make the comparison possible, as it has the following properties[6]:

- $\phi < -\frac{\sqrt{2}}{2} \Rightarrow (\Psi(\phi) = C = 0)$.
- $\phi > \frac{\sqrt{2}}{2} \Rightarrow (\Psi(\phi) = C = 1)$.
- $|\phi| < \frac{\sqrt{2}}{2} \Rightarrow (0 < \Psi(\phi) = C < 1)$.

In the first case, considered computational cell is empty, in the second it is full, and in the third case it is a cell cut by the interface. To actually define Ψ function we must specify how C is computed in nontrivial cells.

If we can approximate implicit Level-Set interface with a straight line, and represent the line with $m_x x + m_y y = \alpha$ equation, we get the dependence

$$\alpha = \frac{\phi}{m^\phi_x + m^\phi_y} + \frac{1}{2} \tag{28}$$

where $m^\phi_{(\cdot)}$ denotes components of vector *normal to the zero-isoline of the Level Set function*. As mentioned above, these normals, given ϕ distribution, can be easily found e.g. using Youngs' scheme. This way, using (28) in nontrivial cell, one can find values of α in a nontrivial cell. [7]

We are now able to find α and $\mathbf{n}^\phi$ for LS interface. We can now use the flux-calculating procedure (dependence (25)), with $u\delta t = 1$ to find the quantity of traced mass delimited by the interface. This will yield the total

[5]Two dimensional $\gamma = 2$. situation is chosen for simplicity of description.

[6]For current examples, we will assume that level set function ϕ takes negative values $\phi < 0$ outside the traced phase, and is positive ($\phi > 0$) inside; this choice is purely arbitrary. Besides, cell indexes are dropped.

[7]The division by level set normals is motivated by condition $m_x + m + y = 1$ held for positive m_x and m_y, under which α can be mapped onto $[0, 1]$.

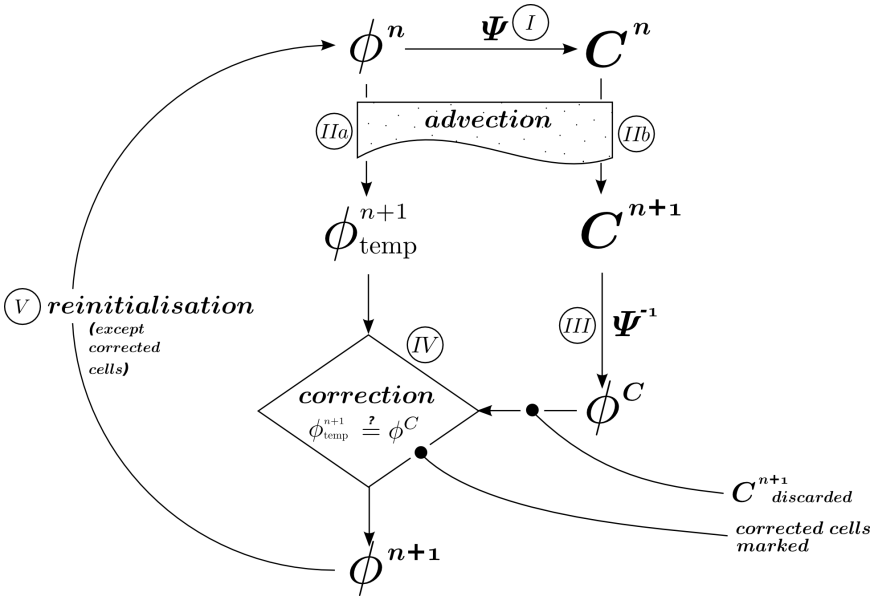

Figure 1: Diagram of a CLSVoF algorithm.

area/volume under the interface, and Ψ will be defined. So to reiterate, Ψ is a combined function, which written with all arguments list would have the form:

$$\Psi(\phi) = Flux(\Psi((\mathbf{n}^\phi(\phi), \alpha(\mathbf{n}^\phi(\phi))), \mathbf{u}, \delta t)) \tag{29}$$

using $u\delta t = 1$ and with $Flux$ being a VOF-specific function (25) used to calculate the fluxes (in (24)) of C, through the walls. This approach seems simpler than least-square minimization approach of [38].

Being equipped with Ψ function, we can generate C^n from ϕ^n and by this finish step I (refer to Fig. 1). Step II.a is an aforementioned advection of ϕ. Now II.b is a VOF advection carried out in a classical manner, just as it would be done in normal VOF-PLIC implementation. In effect, we get C^{n+1}, an advected VOF interface.

The point of CLSVOF – at least in its original formulation – is to compare LS and VOF distributions to enable correction. However ϕ and C are only comparable through $\Psi(\phi) = C$, hence we need Ψ^{-1}. This is step III, using

$$\phi^C = \Psi^{-1}|_\Gamma(C^{n+1}) \tag{30}$$

to generate a level set function directly comparable with ϕ^{n+1}_{temp}. The $|_\Gamma$ designates restriction to the interface. The restricted reverse of Ψ is in fact designed much like the original function, due to the bijection between ϕ and $\alpha(C, \mathbf{n})$ that exists on Γ. Therefore $\Psi^{-1}\colon \Gamma \to [-d, d]$ and

$$\phi^C = \Psi^{-1}|_\Gamma(C^{n+1}) = \alpha(C^{n+1}, \mathbf{n}(C^{n+1})) - \frac{1}{2}, \tag{31}$$

and d is the diagonal of a computational cell.

Construction of Ψ^{-1} on a broader domain is highly nontrivial (although valuable attempts exist i.e by Cummins et al.[10]). Above function allows to calculate $\phi^C\colon =$ $\phi(C^{n+1})$ in interface cells, and for such cells, we will have now clear view of possible differences $\phi^C - \phi$.

The next stage is step IV, i.e. the correction of the level set.

5.3.2. Correction of the Level Set

To correct the values of Level Set, one needs correction criteria, allowing to choose (mark) cells that require correction. We now have computed $\phi^C, \phi^{n+1}_{temp}$ and C^{n+1}. Also, at this point, which on Fig. 1 is marked IV, we generate $C^\phi = \Psi\left(\phi^{n+1}_{temp}\right)$. In our current implementation, the values of ϕ are corrected under the following conditions:

1. $|\phi| < d/2 = h\sqrt{2}/2$
2. $0 + \epsilon < C^{n+1} < 1 - \epsilon$
3. $\phi^{n+1}_{temp} \neq \phi^C$, or $C^\phi \neq C^{n+1}$

with C^ϕ described above. First requirement ensures, that ϕ changes sign inside the cell - as $d/2 = h\frac{\sqrt{2}}{2}$ is the maximal distance from (square) cell of size h to its corner. In other words, ensures that interface is passing through the cell. In general, for cell of size $\Delta x \times \Delta y \times \Delta z$, we need half of the cuboid's diagonal $\frac{d}{2} = \sqrt{\Delta x^2 + \Delta y^2 + \Delta z^2}$.

Second criterion, with ϵ being a small number, is a simple requirement of VoF fraction function non-triviality. This way, even if the limit in criterion 1 is too strong, we can evade treating trivial (full/empty) cells that probably don't need correction. If $1 - C^{n+1} < \epsilon$ (such cell is considered full) and at the same time ϕ indicates empty cell, the correction will not take place. This situation is however considered unlikely as it assumes that a very large discrepancy between VOF and LS interfaces can be created during one timestep.

Third criterion is based on our previous discussion, that values of C originating in VoF advection are more

reliable that C^ϕ. Actually, we can allow these two values to be reasonably close, and correct Level Set only if the difference is bigger than a set value. Authors of [53] advice using $|C^\phi - C| < 0.001$ as a criterion. Also, some of the criteria may not be used at all (or loosened), increasing the number of corrected cells, though it's not profitable to correct in *every* interface cells because it degrades the quality of curvature calculated from level set.

As we have found in our experiments, setting the right criteria is a matter of certain delicacy - ideally only cells in under-resolved areas should be corrected. Setting too broad criteria will cause ϕ values to change everywhere on the interface, while very strict levels may cause no correction at all.

After deciding that a certain cell will be corrected (Fig.1, step IV), we mark it and then simply change its ϕ value to ϕ_c. This finishes most of the procedure; the only remaining step is the reinitialisation/redistancing of ϕ (step V). The important part of CLSVoF algorithm is the omission of marked cells (the ones that underwent correction), so that their ϕ values will not be changed during the reinit.

It is important to note, that in our implementation of the CLSVoF algorithm, the C function is *not* conserved throughout the simulation, but rather recreated from ϕ at the beginning of each timestep. This way, the traced mass may still be lost in reinitialisation of ϕ, we adress this problem by modifying the redistancing procedure[53, 38], however the mass consvation is still inferior to "pure" VOF method. The advantage of CLSVOF is however the possibility to utilize the Ghost Fluid technique.

6. Approximate Deconvolution

The Approximate Deconvolution Model (ADM) was developed by Stolz et al. [50] and applied to incompressible wall-bounded flow. The idea of ADM is to recreate the filtered sub-grid scales of the flow. If the filtering operation is denoted by convolution kernel G, we could denote (for a compact support filter):

$$\overline{u(x)} = G \star u = \frac{1}{\Delta} \int_{x-\Delta/2}^{x+\Delta/2} G(\frac{x-x'}{\Delta}, x) u(x') dx', \qquad (32)$$

where Δ is the filter width. In shortened notation using new variable $z = \frac{x-x'}{\Delta}$ we get

$$\overline{u(x)} = \int_{x-\Delta/2}^{x+\Delta/2} G(z, x) u(x-z) dz. \qquad (33)$$

The three-dimensional form is obtained by filtering independently along three coordinate axes, i.e. as a convolution of three filters G_x, G_y and G_z defined analogously to (32). Furthermore, commutation is assumed between filtering and derivation operations.

The idea of ADM is to calculate τ_{luu} by a simple model - directly , using u_i^*, an approximation of unfiltered quantity u_i. It is therefore a deconvolution class closure, similar to Domaradzki's approach [14]. The deconvolution technique originated in computer graphics, where it was using for 'sharpening' images. One may think of reconstructed function f as being a "sharpened" $\overline{f}$.

Using u_i^* the modeled tensor reads simply:

$$\tau_{luu} = \frac{\partial \overline{u_j^* u_i^*}}{\partial x_i} - \frac{\partial \overline{u_i}\,\overline{u_j}}{\partial x_j}. \qquad (34)$$

Using the above formulas, ADM proceeds to replace u_i with u_i^* in nonlinear terms. It has to be noted that to ensure proper energy drain from resolved scales, original ADM proposed by Stolz et al. [50] uses also the relaxation term

$$-\chi(I - G^{-1} \star G) \star \overline{u_i} \qquad (35)$$

added to the right-hand side of (19), with χ_u being relaxation parameter and G^{-1} denotes the inverse of filter G. Since, as will be explained below, G^{-1} is approximated, this term generally is nonzero. Calculation of (35) has been therefore implemented in the code used for present study.

The approximate inverse of G is based upon analogy between functionals over $\mathbb{L}^2$ space and real functions over $\mathbb{R}$, namely the analog of Taylor expansion. Existence of such a converse of Taylor Theorem has been investigated for example by Dayal & Jain [11].

Approximate inverse G_N^{-1} (of Nth order) of G is, assuming its existence, expressed by

$$G_N^{-1} = \sum_{l=1}^{N} (I - G)^l, \qquad (36)$$

provided that $||I - G|| < 1$, i.e. the series is convergent. In practical application, the expression for G^{-1} is truncated. Adams suggests that setting $N = 5$ gives acceptable results. For example, expanded expression for $N = 4$ would be

$$G_4^{-1} = 4 - 10G + 10G^2 - 5G^3 + G^4, \qquad (37)$$

so that

$$u^* = G_4^{-1} \star \overline{u} = 4\overline{u} - 10G \star \overline{u} + 10G^2 \star \overline{u} - 5G^3 \star \overline{u} + G^4 \star \overline{u}, \qquad (38)$$

where $G^2 \star u = G \star (G \star u)$.

Choice of a particular filter for ADM could, as suggested by Geurts [24], be linked to the fact that spatial discretisation leads to behaviour reminiscent of filtering. It means, that any spatial discretisation induces filtering of all quantities (derivatives) calculated by with it. In that manner Geurts shows an example of first order finite difference scheme inducing a top hat filter of width equal to grid spacing. If that were so while one uses grid-based

LES, it would be desirable that filters used for ADM mimicked the filter-inducing behaviour of spatial discretisation. Intuitively, it would mean that ADM reverses the filtering induced by discretisation. However, filter construction technique proposed in [24] applies only to explicit discretisations, such as finite differences, while SAILOR-LES uses a Páde and pseudo-spectral schemes, with an option to mix the two. We therefore are yet unable to propose analytic formula for discretisation-induced filter G relevant to our simulation, instead we use the explicit fourth order filter that applies a five point stencil, proposed by Stolz et al. [50, 27]

$$\begin{aligned}\overline{f(x)} &= f(x) - (f(x+2h) - 4f(x+h) + 6f(x) \\ &\quad -4f(x-h) + f(x-2h))/16 \end{aligned} \tag{39}$$

7. Calculation of τ_{rnn} Tensor

The capillary tensor, resulting from unresolved interface shape is expressed with (18). The δ_S is computed using condition on the level set, such as

$$\delta_S(\mathbf{x}) = 1 \Leftrightarrow |\phi(\mathbf{x})| < \min(\Delta x, \Delta y, \Delta z). \tag{40}$$

The $\nabla \cdot \overline{\mathbf{n}}$ term in (18) is curvature of the interface calculated from the level set.

As with τ_{luu}, modelling of τ_{rnn} tensor is required since $\mathbf{n}$ is unknown in a Large Eddy Simulation. Thanks to the ADM algorithm, it is however possible to produce quantity that we define as $\mathbf{n}^*$, a vector field of reconstructed normals. This can be achieved in (at least) two different approaches tested during the preparation of this article, which we will now describe:

(A) Direct ('explicit') deconvolution of $\mathbf{n}^*$, i.e. $\mathbf{n}^* = G^{-1}(\overline{\mathbf{n}})$ where G^{-1} is the deconvolution operator.

(B) Indirect ('implicit') deconvolution, based upon assumption that for a given velocity field $u_i(x_i, t)$, the $\mathbf{n}$ field can be represented as dependent from the velocity field

$$\mathbf{n} = f(u_i(x_i, t)), \tag{41}$$

and f is an injective function[8] . In other words there is at least injective dependence between velocity field and the interface shape[9], which seems justified, since the only way for the interface to change its shape is to undergo advection[10]. This way $\mathbf{n}^*$ calculation is realized by finding $\mathbf{u}^*$.

[8]That is, if $a, b \in X$ then $a \neq b \Rightarrow f(a) \neq f(b)$.

[9]Expecting f to be a bijection would be, intuitively, logical with zero boundary conditions and no heat exchange, i.e. in case of flow driven by surface tension and density jump.

[10]It is, however, implied, that $\mathbf{n}^* = \overline{\mathbf{n}}$ whenever there is no flow, e.g. in case of stationary spherical droplet.

Since in (B) approach $\mathbf{u}^*$ is the approximately deconvoluted $\mathbf{u}$, we could follow original approach of Stolz et al. [50] and include $\mathbf{u}^*$ in simulation effectively discarding any sub-grid models used in SAILOR. In this work, however, $\mathbf{u}^*$ is used only for interface advection.

The (B) approach was chosen and applied for most of calculations. The rationale for this is that the deconvolution of the velocity field seems less prone to errors resulting from oscillations caused by high-order filters when processing variables with jumps, such as would inevitably appear in case of normal vectors, which are defined only on the interface. This could subsequently cause errors in resulting τ_{rnn} values.

The (B) variant is implemented as follows. Advection of the interface is carried out twice, once using velocity field $\overline{\mathbf{u}}$, yielding $\overline{\mathbf{n}}$ and once again with $\mathbf{u}^*$ resulting in $\mathbf{n}^*$. Resulting quantities are stored in separate tables and used later to calculate τ_{rnn} using its definition (18).

In the CLSVOF method, there exists a possibility to obtain at any moment both normal vectors calculated from C and from ϕ function. Therefore, similar to CSF approach of Brackbill et al. [8], VOF could be used to obtain $\nabla \cdot \mathbf{n}$ in (18). In our calculations however, the curvature calculation in the Ghost-Fluid procedure utilises $\mathbf{n}(\phi)$, as the LS method guarantees smooth representation of the interface [22]. Therefore, for consistency, we are also using level set-derived normals to calculate τ_{rnn} in (18).

Simple diagram of the τ_{rnn} reconstruction procedure can be seen in Fig. 2. Our computational practice shows that using high-order solver with Conjugate Gradients and Multigrid techniques such as SAILOR, the computational cost of running CLSVOF twice is still merely a fraction of CPU time needed for Poisson equation.

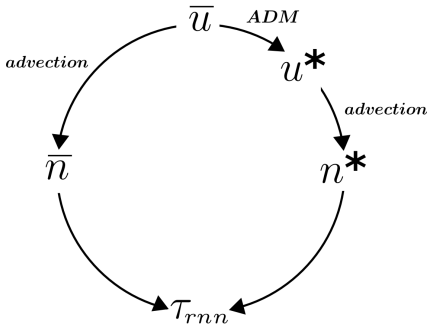

Figure 2: Diagram of the τ_{rnn} calculation algorithm, (B) approach.

Remark Concerning the "Sub-Grid Mass Transfer"

Toutant [58] and Vincent [55] describe, besides τ_{rnn} tensor mentioned here, another term – which is entirely of numerical origin – and emerges when VoF-specific C function transport equation is subject to filtering, namely

$$\frac{\partial \overline{C}}{\partial t} + \overline{\mathbf{u}} \cdot \nabla \overline{C} = 0, \tag{42}$$

contains nonlinear convective term, to which attributed is the term

$$\sigma_1 = \mathbf{u} \cdot \nabla \overline{C} - \overline{\mathbf{u} \cdot \nabla C} \tag{43}$$

which we denoted σ_1 following [55] and refer to it as a *sub-grid mass transfer* (SMT) term, since it involves unfiltered (sub-grid) distribution C. Obviously, usage of levelset ϕ function instead of C does not change anything in this context.

In present authors' opinion, a similar deconvolution-based approach could be feasible for SMT term, however in the present work, modelling of σ_1 has not yet been performed. We agree that it should be subject to future study, as [55] proves that the term has high values in computational case of phase-inversion problem (Section 8.2), relatively to resolved convective term in (42).

8. Numerical Experiments

8.1. Advection Scheme Testing

Some results of three dimensional CLSVOF coupling performance (without ADM model for τ_{rnn}) are presented here. To begin, let us consider a velocity field $\mathbf{u} = (u, v, w)$ defined by:

$$\begin{aligned} u(x,y,z,t) &= 2\sin^2 \pi x \sin \pi y \sin \pi z \cos \pi t \\ v(x,y,z,t) &= -\sin \pi x \sin^2 \pi y \sin \pi z \cos \pi t \\ w(x,y,z,t) &= -\sin \pi x \sin \pi y \sin^2 \pi z \cos \pi t. \end{aligned} \tag{44}$$

This field [38] presents eight artificial vortices in domain octants. Let $x, y, z \in [0, 1]$, and $t \in (0, 1)$, actual role of $\cos \pi t$ coefficient is to change sign when $t = \frac{1}{2}$. Spherical droplet of radius $r = \frac{1}{5}$ is placed inside the domain at point $(\frac{1}{3}, \frac{1}{3}, \frac{1}{3})$. Under such conditions, passive advection of the droplet using (44) is performed. This test is widely presented in subject literature [38, 18, 6], and its purpose is to introduce substantial droplet deformation, by which method's ability to trace thin films, topology changes and its mass conservation capabilities are assessed. If t is allowed to change in aforementioned manner, velocity field will reverse and the droplet will go back to it initial position. However, due to numerical errors, every method introduced some form of an error. Comparison of initial and final droplet shape is therefore – once again – a possibility to qualitatively and quantitatively check method errors.

Let us also notice that for (44), divergence of $\mathbf{u}$ is analytically nonzero, causing the assumption of $\mathbf{u}$ being solenoidal is unfulfilled in derivation of VoF (equation (24)). This in turn may introduce C values outside the interval $[0, 1]$. Combined with "clamping" procedure – in which values of C are restricted to $[0, 1]$, – which is commonly used in split-advection VOF implementations, this may lead to loss of traced mass. In practice, approximately 5% of mass has been observed to be lost for advections carried to the stage depicted in Fig. 3 on coarse 32^3 grid, with smaller values on finer grids. In general, to prevent this, the correction for the divergence is addded to (23), e.g. in [63].

Table 1: The L_1 error for 3D CLSVOF passive advection using velocity field (44).

N	L_1 error	rate	order
16	0.03371	–	–
32	0.0197	1.71	0.855
64	0.00838	2.35	1.175
128	0.00326	2.56	1.28

When t is disregarded, field (44) is strictly steady [5]. Therefore, it has static streamlines, that is solutions of

$$\frac{dx}{u(\mathbf{x})} = \frac{dy}{v(\mathbf{x})} = \frac{dz}{w(\mathbf{x})}. \tag{45}$$

Figure 3(a) presents the shapes of distorted droplet, after it has been advected under (44) and in (b) the result of similar simulation using a pure Levelset method. Droplet shape is presented for $t = \frac{\pi}{2}$, that is exactly at the moment when droplet is most deformed. A thin film of fluid is traced by CLSVOF[11], in contrast to LS, where respective part of mass has been lost. In addition, Figure 4 presents the final shapes of the droplets obtained at $t = \pi$ for the very coarse (32^3) and medium-sized (64^3) grids, enabling the qualitative comparison of results (in Fig. 4, left-hand-side pictures correspond to the results presented in second and third line of Table 1).

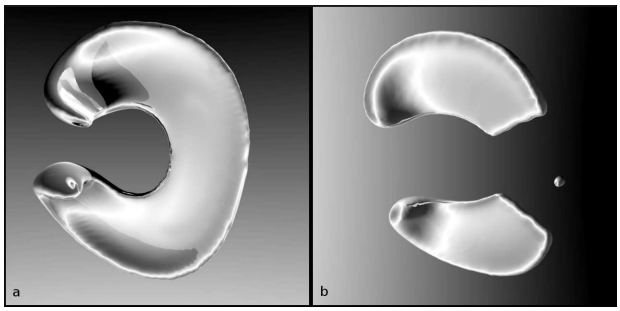

Figure 3: Comparison of method performance: CLSVOF advection (a) and LS advection (b) of a circular droplet under velocity field (44).

For $t = \pi$, the droplet should have returned to its original shape.

To further investigate the performance of the CLSVOF method in passive advection test, we perform the following test using velocity field (44). The droplet was advected from, and returned to its starting position, since the term $\cos \pi t$ in (44) changes sign as $t > 0.5$. Initial and final droplet shapes differ, depending on the performance of the advection method applied. The difference may be quantified using L_1 error. To present exact error formulation,

[11] Analysis of layer thickness is widely covered in [38].

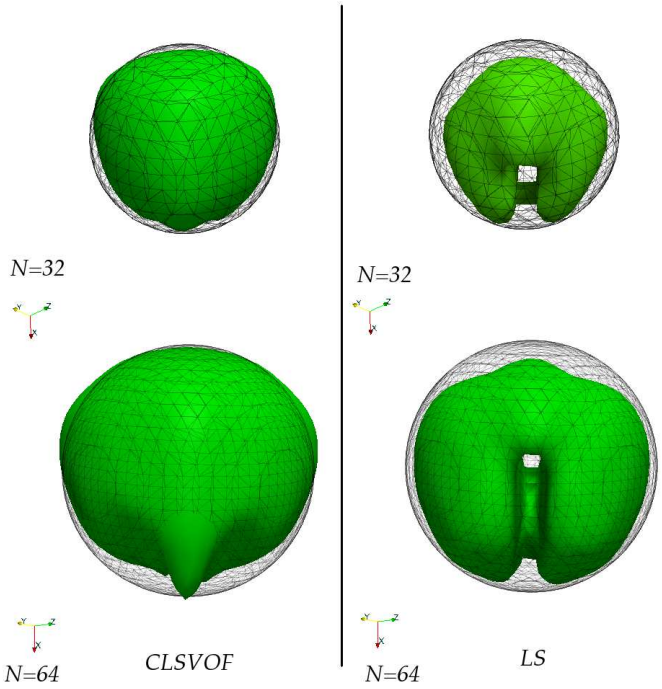

Figure 4: Final shape of the droplet, for CLSVOF and LS methods. Wireframe delineates original ($t = 0$) shape, while green isosurface depicts final shape ($t = \pi$)

let us introduce following symbols: N as a number of grid nodes in uniform grid (with N^3 nodes), (i, j, k) as index of grid cell, with all three indices ranging from 1 to N. Then

$$L_1 = \frac{1}{N^3} \left(\sum_{i,j,l=1}^{N} |C^0_{ijk} - C^f_{ijk}| \right), \tag{46}$$

with C^0 standing for the initial, and C^f the final distributions of the VOF fraction function C. Normalizing by N^3 is a simple technique to assure that errors are comparable. Results of this numerical test are presented in Table 1. The "rate" column is an estimation of error decrease between consecutive table rows [41], so that for example

$$\frac{L_1|_{N=32}}{L_1|_{N=64}} = \frac{0.0197}{0.00838} \approx 2.3$$

is visible in third row. From this estimation, we can see that the method (that is, the advection scheme) is approximately first order in accuracy, $O(N)$.

For the results presented in this subsection, Parker & Youngs' [40] method is used for calculation of the normal $\mathbf{n}$ to the interface. Therefore, first-order accuracy is expected for VOF method and fully consistent with the results of Pillod and Puckett [41].

When plotted against the dimensionless time, the L_1 error (Fig. 5a) shows that for $N = 16$ the curve does not return to zero value. This is caused by the fact that with this drastically coarse grid resolution, most of the mass have been lost by the time the droplet returns to its original position[12]. Two peaks on Fig. 5a are caused by geometry of field (44), that is: the droplet leaves its initial location (first peak - high error), then it undergoes severe deformation, causing parts of it to coincide with its original location (error drops), which takes place for $t = 0.5$. After this, the process returns to its original state (second peak, and return of error to zero value).

The issue of mass conservation in this case can be studied by inspecting Fig. 5b, in which mass conservation is plotted, as the percentage of droplet's initial mass. Calculation of plotted value is made possible by calculating

$$M(n) = \sum_{i,j,l=1}^{N} C^n_{ijk}, \tag{47}$$

where n stands for the n-th step of temporal discretisation. Value plotted in Fig. 5b is therefore $M(t)/M(0)$. It is visible that while $N = 64^3$ grid results in reasonable mass conservation (90% of initial mass), on the finest grids overshoots are created. Such a mass loss would seem unlikely in pure VOF method (where the sum (47) is constant by definition), but in CLSVOF it can be attributed to the process of re-creation of VOF distribution after every advection step.

While values for mass conservation over 90% may be perceived low compared to machine-precision VOF conservation, it exceeds values obtained by using LS method [39]. Moreover, results presented by other authors [38, 36, 18, 63] show that velocity field (44) is very demanding – when the ability of a given method to conserve mass is considered – grids used by these authors are relatively fine, up to the level of $N = 200$.

An additional, similar test has been performed using a simpler velocity field, namely

$$u(t) = v(t) = w(t) = \cos(\pi t), \tag{48}$$

which was spatially constant. The droplet was placed in point $(0.3, 0.3, 0.3)$ of an $[0, 1]^3$ domain. Passive advection in (48) is equivalent to movement of the droplet to the opposite corner of the domain, and then back to the original location. This simple example is an excellent test for VOF-based advection schemes, similarly to many tests basing on advecting droplets along axes, advection over periodic walls for many periods and similar cases [1].

Analogically to the previous tests, advection on four similar grids have been performed – however, quantitive visualizations of these will be omitted, since the difference between initial and final droplet positions are very small. Instead, we present error analysis in Table 2. From the table, it is visible that in this case a slightly higher error decrease rate is observed, nearing second order between grids 32^3, however does not hold between grids 64^3 and

[12] The CFL condition is utilized to calculate timestep for each grid size. Hence, different timestep dt is obtained and the number of numerical timesteps is not identical.

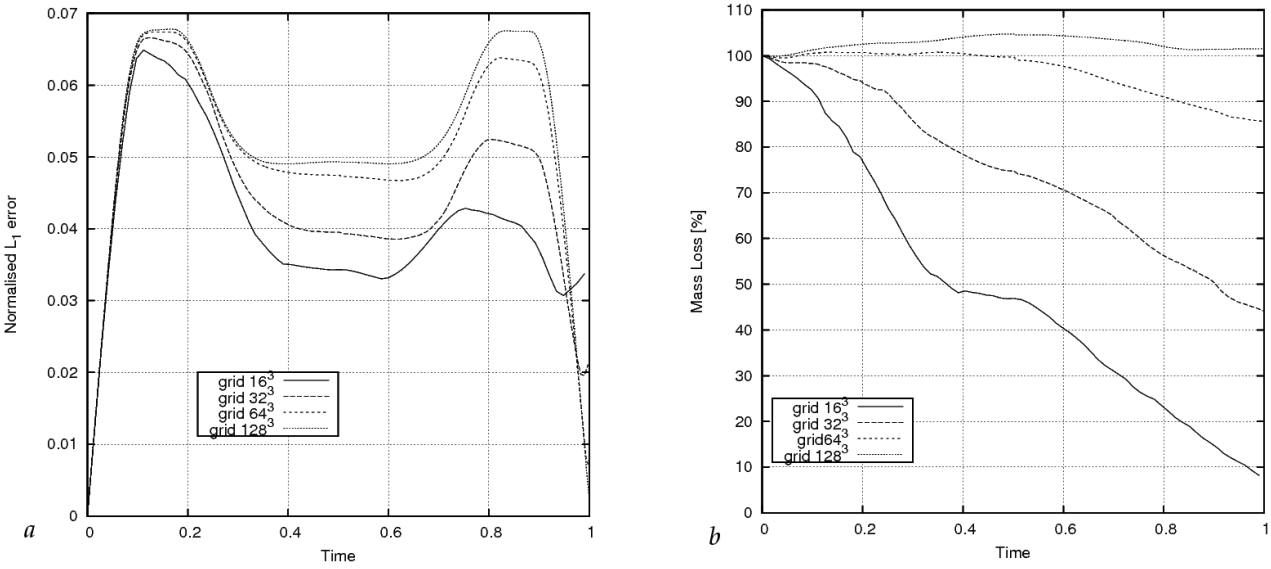

Figure 5: Temporal evolution of (a) errors, (b) normalized dimensionless mass for velocity field (44).

Table 2: The L_1 error for 3D CLSVOF passive advection using velocity field (48).

N	L_1 error	rate	order
16	$4.625 \cdot 10^{-3}$	–	–
32	$1.442 \cdot 10^{-3}$	3.207	1.6
64	$3.729 \cdot 10^{-4}$	3.866	1.93
128	$2.511 \cdot 10^{-4}$	1.485	0.724

128^3. This behaviour is comparable to observed by Sussman et al.[53], who describe CLSVOF algorithm that exhibits interchangeably first- and second-order accuracy in parts of temporal evolution of simulation.

Unlike (44), field (48) has divergence zero, hence much lower mass loss is expected. Indeed, as can be observed in Fig. 6 mass conservation for 64^3 grid reaches 99%, while even for the coarsest 16^3 grid over 80% of mass is conserved unlike in the previous test, when this very coarse grid performed on the 20% level. Result for the 128^3 grid is not pictured, since the value is constant and equal to 100%.

8.1.1. The Calculation of Curvature

As was said, the curvature κ is calculated directly from the level-set ϕ function by using a second order differences scheme. A geometrical analysis of the curvature calculation scheme was performed in two parts: a static test and "parasitic currents" analysis. For a static test, the curvature of a spherical ϕ distribution defined by setting $\phi = \sqrt{x^2 + y^2 + z^2} - 0.1$ was found using our scheme, with the error defined from the knowledge of analytical curvature

$$\kappa = \frac{1}{\sqrt{x^2 + y^2 + z^2}}. \tag{49}$$

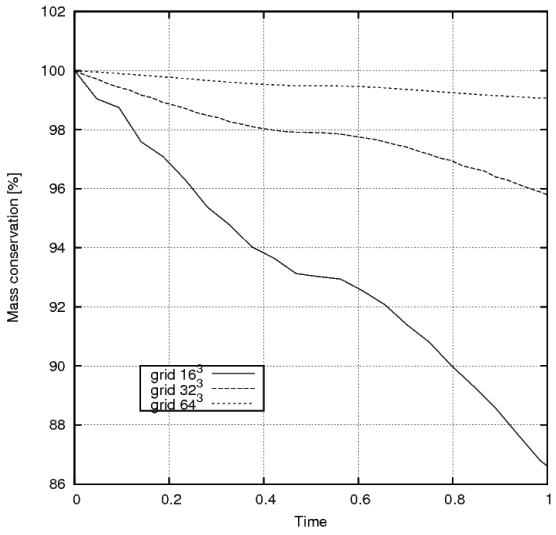

Figure 6: Dimensionless mass temporal evolution for velocity field (48), normalized by the initial value.

Such ϕ distribution corresponds to a sphere of radius 0.1 however, it is obviously possible to calculate κ (as well as calculate ϕ normal vectors) regardless of the position of the zero level-set. The sphere was placed in the centre of box domain of dimensionless size $L = 1$, using varying number of grid cells in each direction. Curvature measurement was performed at three radii chosen from $[0, 0.3L]$ interval. The results, together with an order estimation, are presented in Table 3.

The investigation of "parasitic currents", which are the numerically induced non-zero velocities that arise due to errors of curvature calculation schemes [43] was performed in a following manner. A fully coupled SAILOR-CLSVOF code was used, with 3D domain of nondimensional size

Table 3: Error calculation for static curvature test with order estimation.

N	0.05L	0.15L	0.3L	order
20	3.4×10^{0}	0.2×10^{0}	2.3×10^{-2}	–
40	1.1×10^{0}	4.6×10^{-2}	5.8×10^{-3}	1.6
80	0.3×10^{0}	1.2×10^{-2}	1.5×10^{-3}	1.9
160	7.8×10^{-2}	2.9×10^{-3}	3.6×10^{-4}	1.95

$L = 5.0$, using 64^3 uniform grid. A spherical droplet of radius 1 was placed in the center of domain, defined by the initial ϕ distribution analogous to a 2D example presented above for curvature calculation. There was no jump in density ($\rho_1 = \rho_2 = 1.$) nor viscosity ($\mu_1 = \mu_2 = 0.005$). Surface tension coefficient has been set to $\sigma = 0.375$, and gravity is zero. Under such conditions, we have accepted $max(|\mathbf{u}|)$ measured in domain as an estimation of parasitic currents phenomenon. The maximum was found in whole domain at given moment of dimensionless time t.

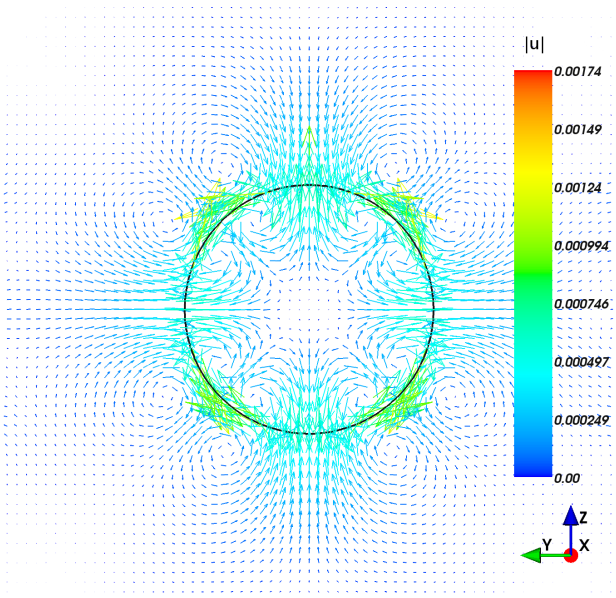

Figure 7: Vector cutplane of the parasitic current distribution for $t = 0.211 \cdot 10^2$.

Symmetrical distribution of the parasitic currents obtained for the CLSVOF code at $t = 0.211 \cdot 10^2$ can be seen in Figure 7. As can be observed, most of the visible vectors are of order 10^{-4}, while the domain-averaged $|\mathbf{u}|$ value was of order 10^{-7}. This is comparable with published results [38] and [20][13], also relates well to data available in [59].

Temporal evolution of the $max(|\mathbf{u}|)$ can be observed in Fig. 8a, prepared on a 64^3 grid. As can be seen in this Figure, oscillations occure which are dumped in the presence of viscosity. Average value of $max(|\mathbf{u}|)$ is of order 10^-3 with a decreasing tendency as t progresses. The

[13] Where similar Ohnesorge number was analised, but 2D advection was considered.

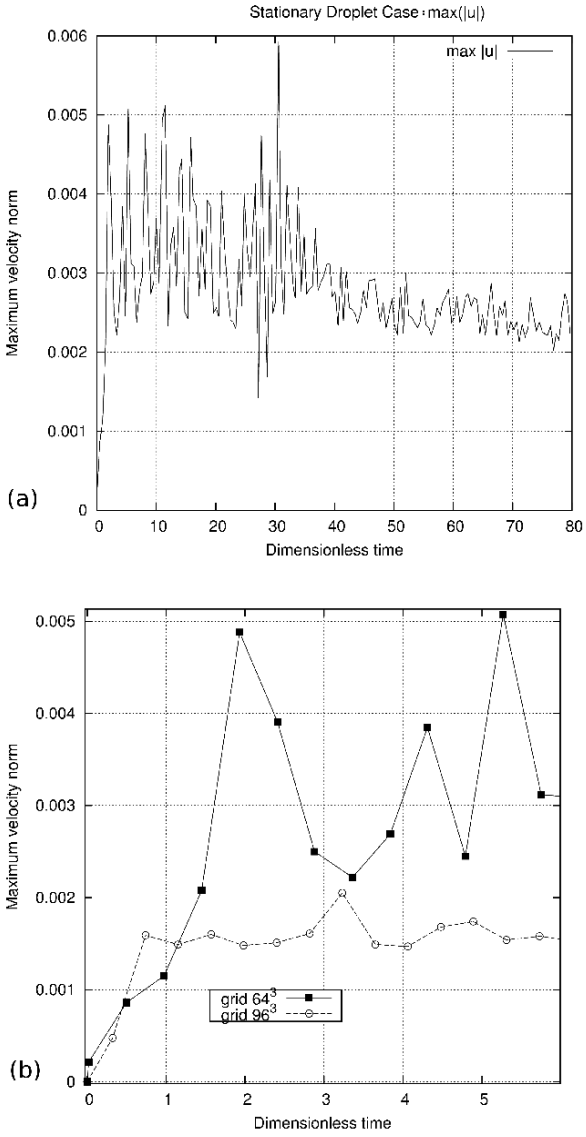

Figure 8: Temporal evolution of spurious velocity maximum for the stationary droplet test case using 64^4 grid.

plot was prepared using aproximately $5 * 10^3$ iterations of the solver, with each value for $max(|\mathbf{u}|)$ searched in entire domain and saved every 10 iterations. This maximum values are consistent with data presented in Figure 7. Additionally, Figure 8b presents a detailed view of temporal $max(|\mathbf{u}|)$ evolution for $t \in [0, 10]$, for both 64^3 and 96^3 grids. A substantial decrease by approximately 60% in median value of $max(|\mathbf{u}|)$ is seen as the grid changes from 64^3 to 96^3.

8.2. The Phase Mixing

Much attention was devoted by the present authors to the computational case of phase mixing ("oil" and "water"), under the mechanism of Rayleigh-Taylor instability. A similar 3D DNS simulation has been performed by authors of [55] (and previously, a 2D case had been described

in [30]). A parametric study for the same case has been published by Toutant [58]. These articles presented *a priori* DNS studies[14] of magnitude, temporal evolution and parametric dependence of sub-grid tensors for LES, among which τ_{rnn} tensor which is the subject of our modelling efforts in this article. It is therefore essential to compare the results obtained by use of ADM-based τ_{rnn} model with mentioned works.

Basic description of the computational case is the following. In a cubical box of side length $L = 1$ m , two phases are initially positioned in such way, that a lighter phase (oil), with $\rho_o = 900$ kg.m^{-3} occupies a cubic subset placed in octant closest to $(0, 0, 0)$ point. The other, heavier phase (water) with density of 1000 kg.m^{-3} fills the rest of the domain. See Fig. 9 for reference. Authors of [55] set $\left(\frac{1}{2}L\right)^3$ as oil cube dimension, whereas in our simulations it is most often $\left(\frac{2}{3}L\right)^3$, which we motivate by our intention to yield greater interfacial surface on coarse grids which cause poor mass conservation. It has been found that characteristics of τ_{rnn} – such as its domain-averaged magnitude presented below – do not change quantitatively due to that scaling. All physical parameters have been set identical to the reference work [55], that is the viscosities of water and oil are respectively 0.001 and 0.1 Pa·s, and surface tension is set to 0.075 N·m^{-1}.

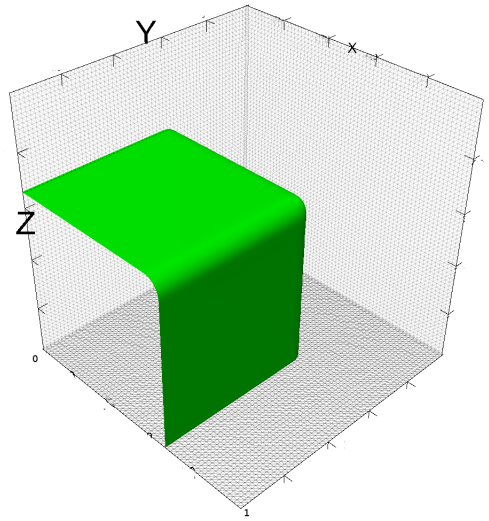

Figure 9: Initial positioning of oil (green surface) and water (rest of the domain) phases in a phase-reversion numerical simulation. Gravity is along vertical Z axis.

Three different grids have been used, namely $32 \times 32 \times 32 = 32^3$ grid (32768 nodes), the 64^3 grid with 262144 nodes, and the 96^3 grid with 884736 nodes. Most of calculations were performed on 16-processor clusters, containing 2210MHz AMD Opteron processors, and 32 GB of RAM. All simulations were prepared using SAILOR-LES solver, using the Smagorinsky model for τ_{luu}, and CLSVOF module for interface tracking; GFM technique was applied to implicitly treat pressure and density jumps on the interface.

Figure 11 displays temporal macroscopic evolution of the interface. Visible in the figure is the large-scale movement of lighter phase upwards, caused by buoyancy force, after which it hits opposite corner of the domain (also see Fig. 15), causing large vortical structures to emerge, which subsequently leads to creation of small-scale interfacial structures, such as droplets and ligaments, best resolved on the finest grid. However, it is evident from inspection of Fig. 11 and 10 that overall number of structures is smaller than described in DNS simulation [55] (obtained using 128^3 grid and the VOF method).

Figure 10: Interface shape for $t = 7.6$ obtained on the 96^3 grid.

Authors of [55, 30, 58] use dimensionless number Re, defined using domain size as characteristic dimension and varying approaches towards characteristic velocity. Let us now review these approaches and apply them to presented computational case. Larocque et al. [33] defines Re as

$$Re = \frac{\rho_w L U_g}{2\mu_w} \tag{50}$$

using "predicted velocity" U_g defined with

$$U_g = \frac{\rho_w - \rho_o}{\rho_w}\sqrt{\frac{gL}{2}}. \tag{51}$$

This time-independent quantity is therefore calculated using only species density and characteristic measure L equal to the domain size [33]. For varying viscosity and surface tension coefficients, [33] describes Re between 1110 and 554000] in their simulation. In the discussed simulation, when calculating using (51), we get value of $Re = 72827$.

It is clear that Re is time independent in such interpretation; in contrast, Vincent et al. [55] define Reynolds

[14] Using VOF method for interface tracking.

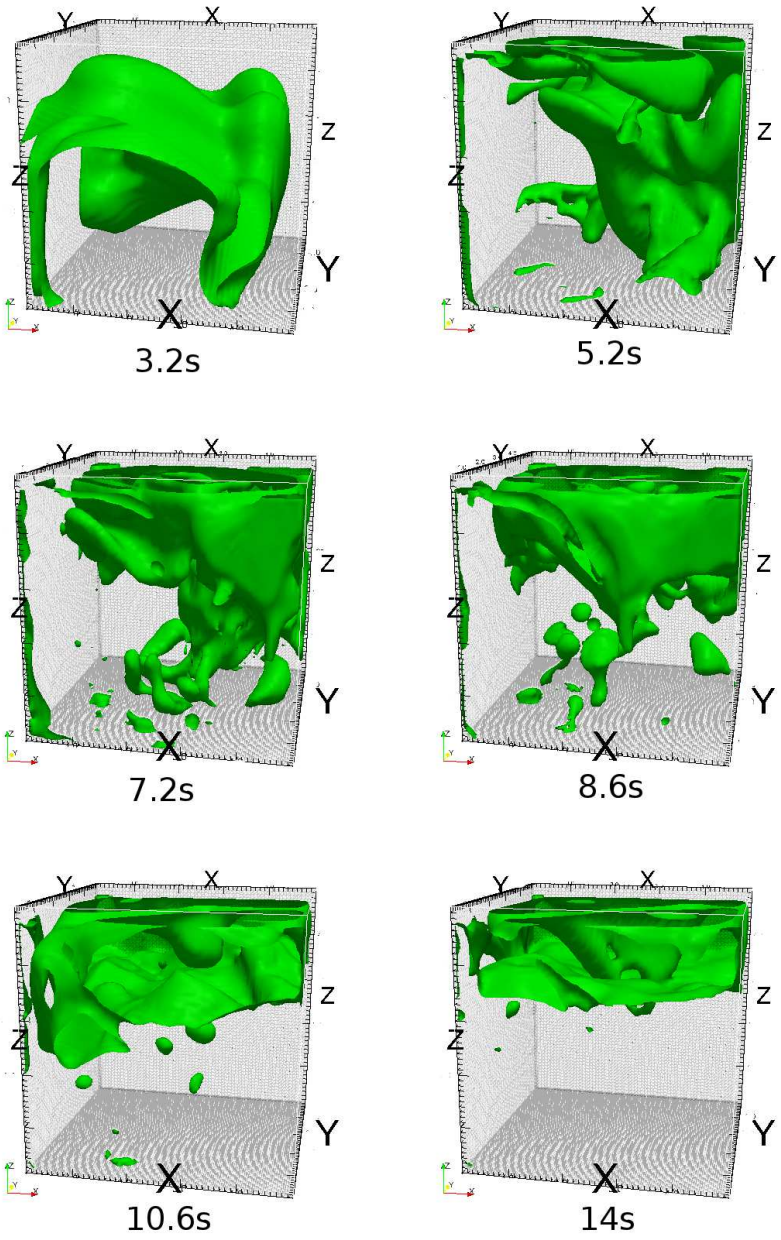

Figure 11: Macroscopic evolution of the interface for oil-mixing test case using a 64^3 grid.

number using maximum of $\mathbf{u}_w$ (in water) at every time-step, and water viscosity, resulting in values up to 60000. In our work, when using $\max \mathbf{u}_w$, very high Re values are observed (up to $3.5 \cdot 10^5$). In Fig. 12, Re values are plotted obtained using $\max \mathbf{u}_w$ (continuous line). These Reynolds number values, much higher than described in [55], are caused by different definition of characteristic scale L. In [55] time-dependent value of L is used, described by authors by "size of larger eddy structures", equal to the macroscale of turbulence [54]. Similarily to (50), in preparation of Fig. 12 constant $L = 1$ has been used.

The second (squared) curve in Fig. 12, is Re calculated using domain-averaged $\langle \bar{\mathbf{u}} \rangle$ magnitude, which yields Re at 10^5 level. Averaging is performed in a way similar to presented in [55], that is

$$\langle \Psi \rangle = \frac{1}{V} \int_V \Psi dV \tag{52}$$

where Ψ is an arbitrary scalar field and V is computational domain, discretisation of Ω.

These levels of Re below 10^5 are in agreement with constant "expected" values yielded by formulas (50) and (51).

Interfacial surface has been traced during our simula-

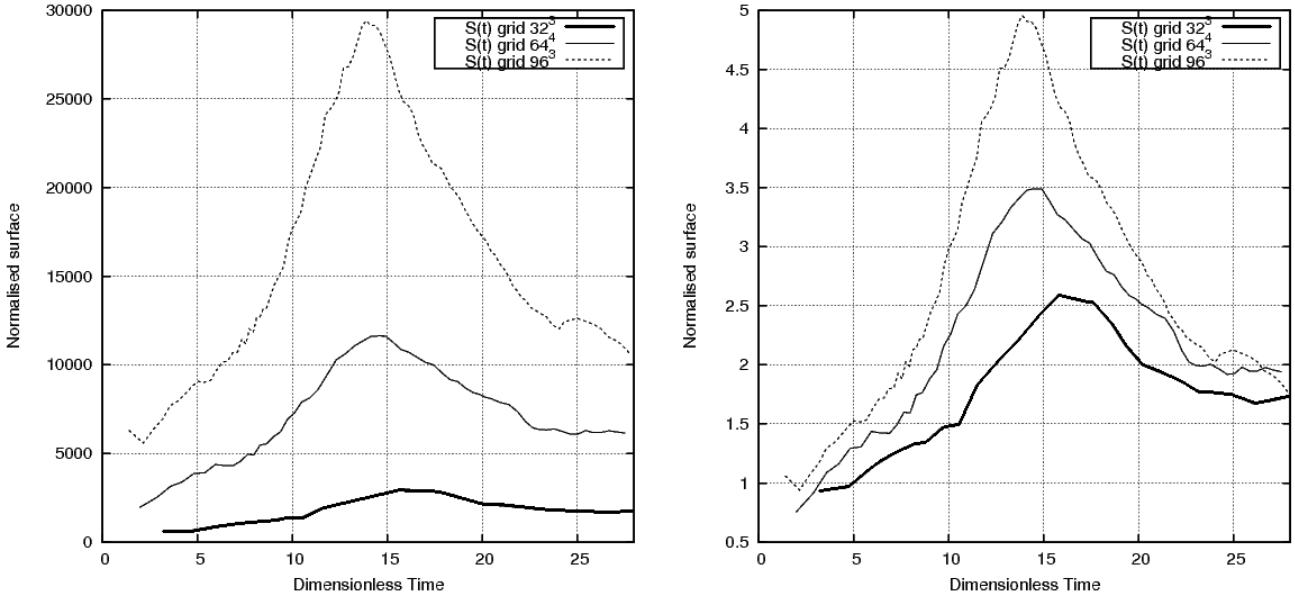

Figure 13: Approximated interfacial area; temporal evolution for phase mixing case. Raw cell count (left) and values normalized by initial interfacial cell count (right).

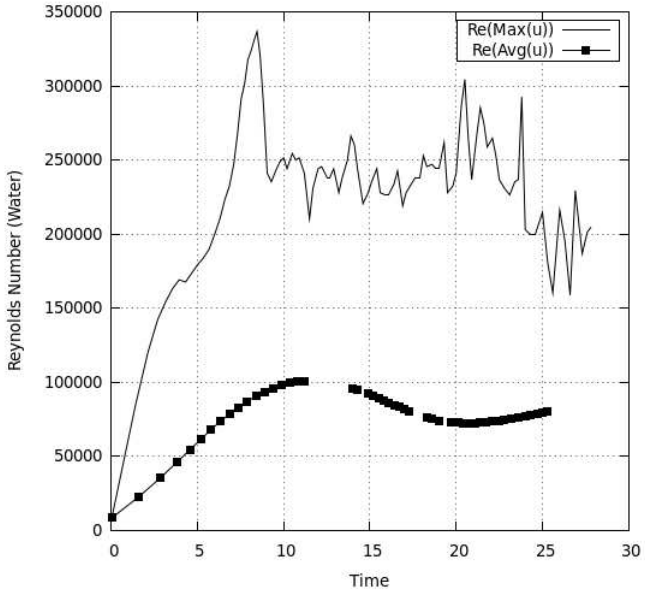

Figure 12: Reynolds number in water temporal evolution. Time units: 1/5 s.

tions, similarly to previous subsection, and the results are given in Figure 13. Interfacial area has been calculated using simple approximation described in [37], that is as a number of cells with $|\phi_{ijk}| \leq d$, where $d = \Delta x/4$. In other words, this approach counts cells with values of level-set ϕ function small enough to assume they contain the interface. Such approach, however crude, is reminiscent of [55], where authors propose a technique based on VOF C function values. Neither of such approaches involves any geometrical reconstruction of the interface, and thus are equally dependent on discretisation and can be perceived only as rough approximations of surface area. Notwithstanding this possible lack of precision, we may observe that overall trend is present in Fig. 13 of surface area rising to approximately 5 times its original value on a 96^3 grid, while on more coarse grids is characterized by less steep decrease following peak values. In particular we see that highest interface fragmentation took place at about 15 time units. Below, data presented in Fig. 13 will allow us to seek correlations between surface area and values of sub-grid surface tension tensor.

Note that for different parameters such as smaller "oil" phase density (or greater "water" density), kinetic energy resulting from buoyancy will be inversely proportional to ρ_o and thus cause interfacial surface to be greater by causing stronger oil fragmentation. The same behaviour, but pertaining to interfacial sub-grid term τ_{rnn} is visible in parametric DNS study of Larocque [33].

Examples of velocity field visualizations for a 96^3 grid are visible in Fig. 14 (leftmost image) and Fig. 15. Latter figure displays the scale of vortical motion in the most kinetic part of simulation, right after the overturned oil mass hits opposite domain corner. In the figure, only half of the interfacial surface is visible as a wireframe. Vectors of velocity in 15 are rescaled accordingly to their magnitude, while in Fig. 14 similar scaling has been performed by much smaller coefficient, to produce clear image.

Figure 15 contains velocity cut-plane parallel to z axis which contains $x = y$ line. The visible part of the interface lies in $y < x$ part of the domain.

In Fig. 14, a $y = 2.5$ cut-plane has been drawn. Apart from representing velocity vector field, Fig. 14 contains (rightmost image) graphic representation of τ_{rnn} vector

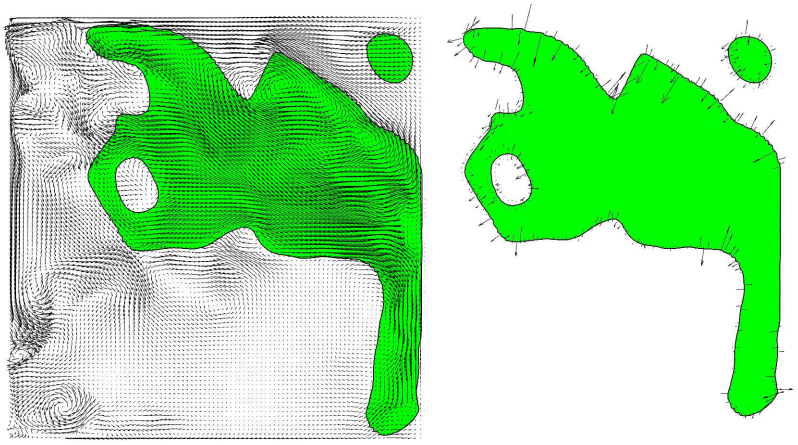

Figure 14: Two cut-planes $y = 2.5$ with vectors of velocity (left, vector magnitude reduced 0.4 times) and τ_{rnn} (right, vectors enlarged 10 times). Both snapshots were taken for $t \approx 20$. Are inside "oil" phase is colored green.

field, taken at the same moment of dimensionless time.

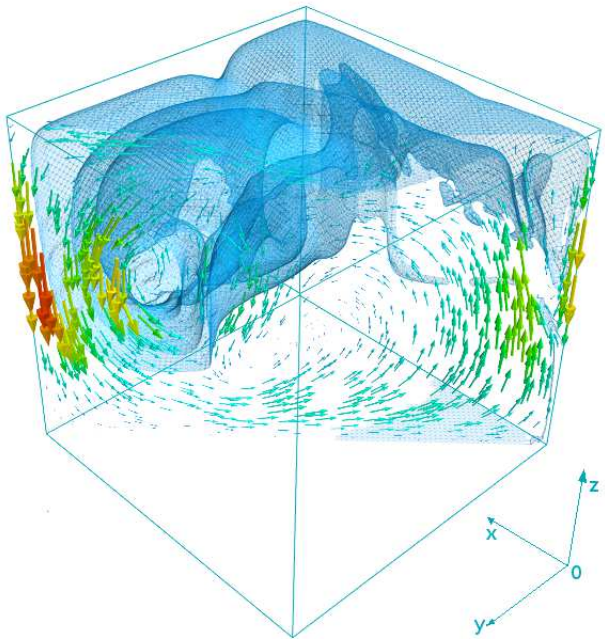

Figure 15: Example of velocity vectors drawn along with wireframe interface representation.

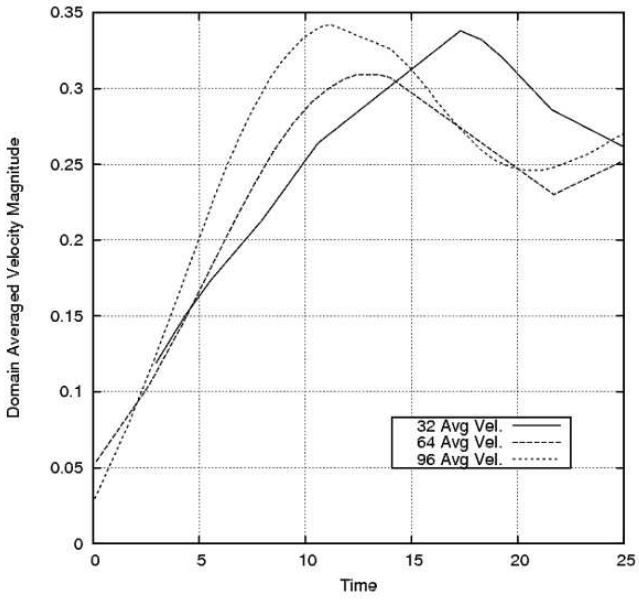

Figure 16: Domain-averaged velocity (m/s) distribution in discretisation dependence in $\rho_o = 900$ kg.m^{-3} case.

Velocity field characteristic was presented in Fig. 12; to further characterize resolved $\bar{\mathbf{u}}$ field we additionally present the plot of the domain-averaged velocity distribution $\langle \bar{\mathbf{u}} \rangle$ for three considered grids in Fig 16. During first 10 time units, acceleration due to overturning motion is clearly visible in all cases. Subsequently the velocity drops, as oil and water masses begin quasi-periodic [55] sloshing movements during which any remaining kinetic energy is dissipated by viscous effects.

In Fig. 17 non-rescaled, averaged components x, y and z of τ_{rnn} tensor are plotted. Visible are curves for 64^3 and 96^3 grids, for $t \in [0, 25]$. As the curves for $\langle \tau_{rnn}|_x \rangle$ and $\langle \tau_{rnn}|_y \rangle$ show, the x and y components do not rapidly increase during the simulation, while $\langle \tau_{rnn}|_z \rangle$ forms peaks visible in interval $[10, 25]$ of both plots. Reason for this is linked to dominating character of buoyancy force in simulation, as overturned mass of oil ruptures into droplets. DNS simulations show great fragmentation in this phase [33] followed by dispersed flow which was not captured in present LES simulations, due to mass loss and numerical coalescence; however medium-sized and large interfacial formations are captured. It is to these formations that peak $\tau_{rnn}|_z$ values seem linked, as concluded by Vincent in [55]. Still, in parts of the simulation where z-direction peaks do not occur, all components act similarly, and overall averaged norm of τ_{rnn} remains at constant level, a behaviour which we will describe below. Large peak of

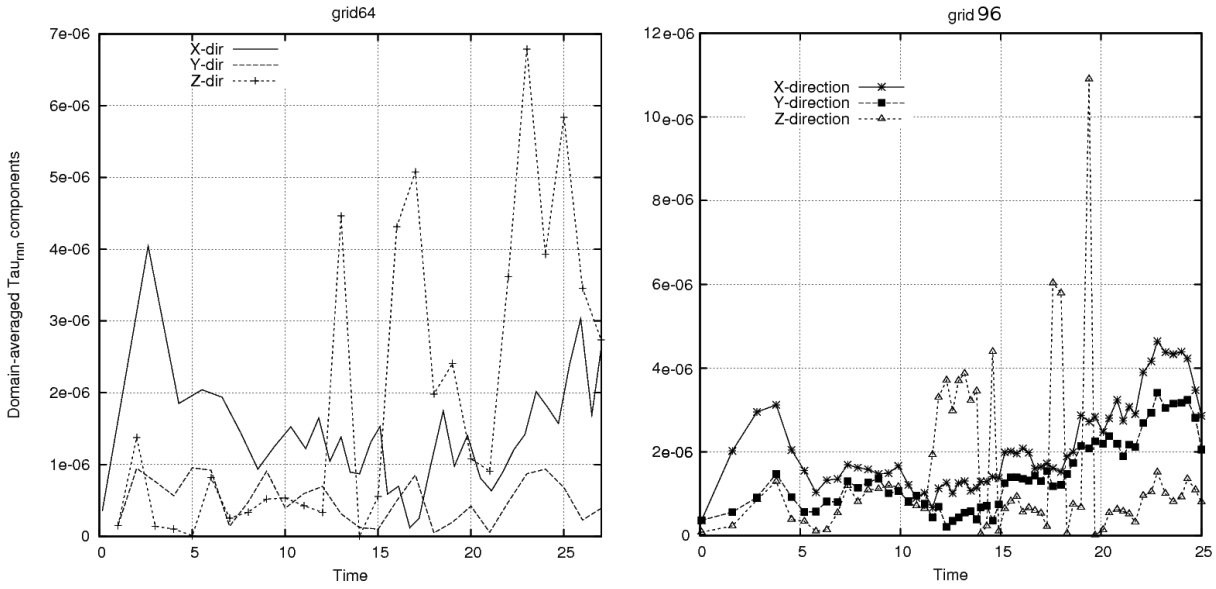

Figure 17: Temporal evolution of $\langle \tau_{rnn}|_{x,y,z} \rangle$ components, no scaling.

$\langle \tau_{rnn}|_x \rangle$ curve in $t \in [0, 5]$ interval visible in both plots of Fig. 17 may be connected to movement of oil drop towards opposite domain corner at the onset of simulation.

In Figure 18a, the maximum values of τ_{rnn} tensor are presented. The graph has been prepared for simulation on 64^3 grid, using $\rho_o \colon \rho_w = 0.7 \colon 1$ ratio, which the results in more emphasized overturning motion and more interface defragmentation. Contrary to what may have been expected from averaged values, maximum levels are of order 10^{-1}. Highest values (x-component peak at $t = 16.4$) are once again connected with interfacial rupture phase in $t \in [15, 20]$ interval, during which the mass divides into bulk part that forms large ligament that later ruptures into droplets. We have traced spatial location of peak tensor value, which is shown in Fig. 18b as being connected with interface cusp.

Concerning surface tension coefficient σ, it is important to remind that σ is present in definition (18) of τ_{rnn} and any change to σ will cause τ_{rnn} to directly re-scale. However, some characteristics of the flow in the discussed case would also change then, e.g. greater surface tension will produce different, less fragmented oil mass configuration, also influencing the average velocity of the overturning motion. At the same time, τ_{rnn} will become larger due to scaling by σ. Because of that and other reasons – such as the need to assess importance of two-phase specific terms altogether – ratio of τ_{rnn} components might be calculated versus some flow-specific quantity, as mean velocity or flow inertia. Such ratio was used in [55].

In our work, we have assessed the significance of τ_{rnn} by comparing its norm with that of the domain-averaged resolved inertial term

$$\rho \overline{\mathbf{u}} \otimes \overline{\mathbf{u}}, \tag{53}$$

computed directly in simulation. The ratio of

$$\frac{\tau_{rnn}}{\rho \overline{\mathbf{u}} \otimes \overline{\mathbf{u}}}$$

is a dimensionless quantity, directly comparable with plots presented in reference works [55] and [30]. Moreover, it may be seen as a comparison between tensors τ_{rnn} and τ_{luu} (that is the "classical" SGS tensor (12)) . When making the plots, we have used either the ratio

$$\frac{\langle |\tau_{rnn}| \rangle}{\langle ||\rho \overline{\mathbf{u}} \otimes \overline{\mathbf{u}}|| \rangle}, \tag{54}$$

of tensor norms, or ratios using components of sub-grid surface tension tensor such as

$$\frac{\langle \tau_{rnn}|_z \rangle}{\langle ||\rho \overline{\mathbf{u}} \otimes \overline{\mathbf{u}}|| \rangle}. \tag{55}$$

Averaging operator $\langle \cdot \rangle$ was described in previous subsection. In the above equations, we have used Euclidean norm (Frobenius norm) of the matrix in the denominator, namely, for an arbitrary matrix $\mathbf{A}$:

$$||\mathbf{A}|| = \sqrt{\sum_i \sum_j |a_{ij}|^2}. \tag{56}$$

In Figure 19, an actual time dependence of fractions (54) and (55) can be seen. Figure 19 has been prepared using least refined grid 32^3, and indicates a constant rise in plotted value, reaching 7% of approximated inertia for $t = 16$ s. This is comparable to values described in [55], in which the authors give e.g. the value of (55) at about

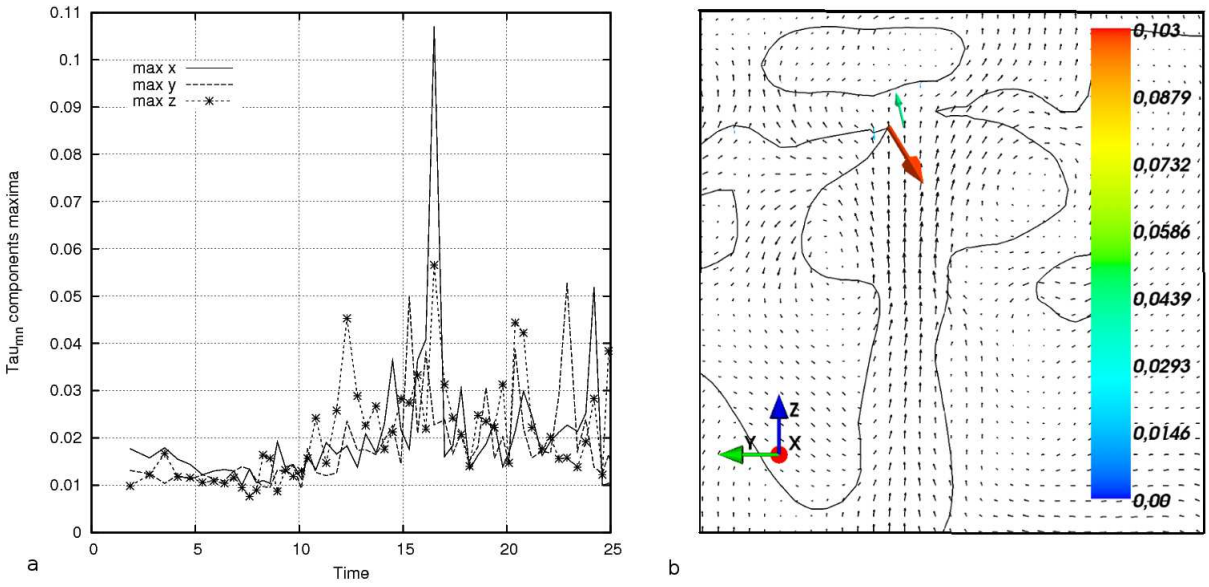

Figure 18: (a):Temporal evolution of $\max(\tau_{rnn}|x)$, $\max(\tau_{rnn}|y)$ and $\max(\tau_{rnn}|z)$ for oil mixing simulation. No averaging was performed. (b): Cutplane drawing for $t = 16.4$, matching peak value in (a). Red vector (unscaled) represents peak τ_{rnn} vector, also visible is 2D zy cutplane of the interface (thick black line), and velocity field visualization (downscaled black vectors).

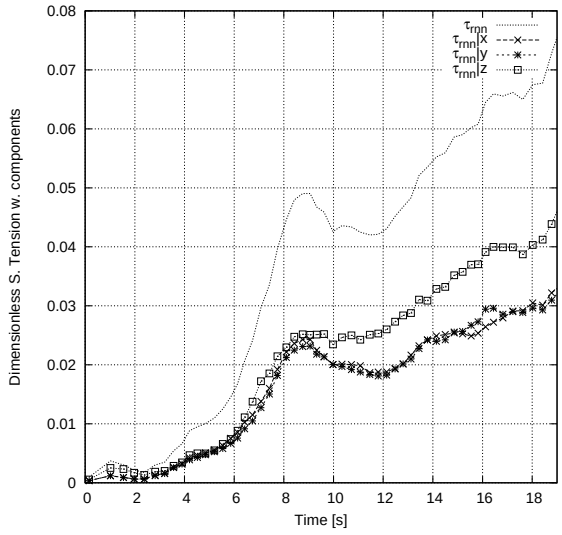

Figure 19: Average normalized magnitude of τ_{rnn} tensor and its components, non-dimensional, concerning the simulation on a 32^3 grid.

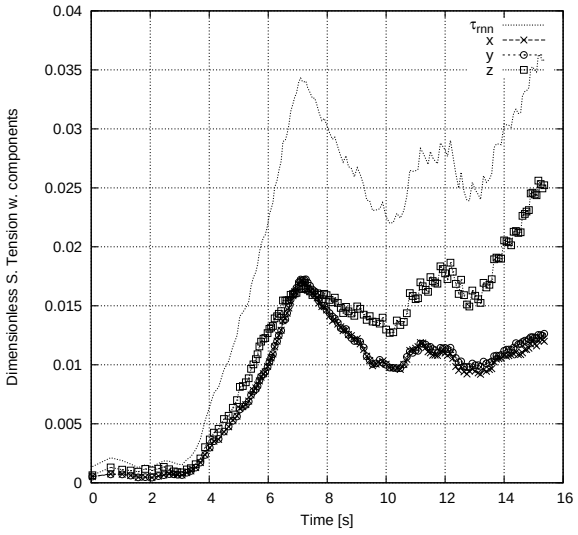

Figure 20: Average normalized magnitude of τ_{rnn} tensor and its components, non-dimensional, concerning the simulation on a 64^3 grid.

5% level for $t = 15s$. Also, Figure (19) shows the values of individual tensor components in the same simulation - the domination of the z component (due to buoyancy force generating the flow) is well pronounced, which again reflects the *a priori* DNS results. It shows that ADM-based reconstruction approach to τ_{rnn} tensor allows for sensible reconstuction of the sub-grid surface tension force, whose magnitude measured with respect to (53) raises as the flow moves to the viscous dissipation phase.

As we can observe in Figure 20, the behavior of the model is similar when a denser, 64^3 node grid is used; we observe a raising value of ratio (54) and the shape of the curve is similar to Fig 19 with a pronounced peak for $t \approx 7s$. This peak is linked to a large value of the interfacial surface, as can be seen in Fig. 21. Overall values of plotted ratio for τ_{rnn} tensor are about 60% of values for 32^3 grid (Figure 19 and 23), which could be attributed to decrease of difference between $\mathbf{u}$ and $\mathbf{u}^*$ velocity fields (and subsequently between the filtered and reconstructed normal vector fields) due to the fact that the flow is less

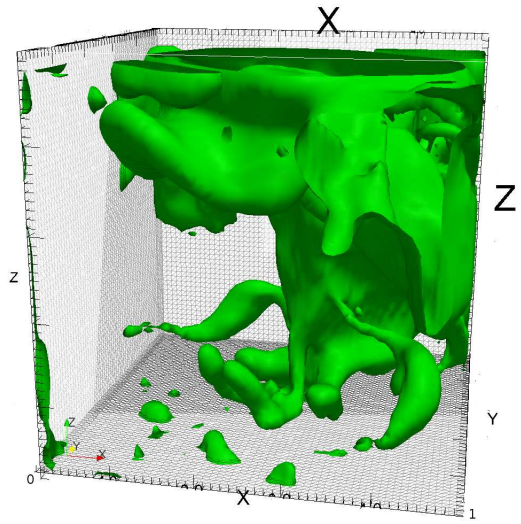

Figure 21: Interfacial surface for $t \approx 7$s in a 64^3 simulation, corresponding to peak value in Fig. 20.

under-resolved. The level of $\tau_{rnn}|_z / ||\rho(\mathbf{u}\otimes\mathbf{u})||$ is comparable to what is indicated in the DNS *a priori* test, and also its domination over other components is in full agreement with published work of Vincent [55]; it becomes even more apparent towards the end of the plotted time interval. To offer more insight into this particular simulation using 64^3 grid, we attach a more detailed view of concurrent interface shapes, visible in Figure 11.

Finally, similar in character and observed magnitudes is the evolution of the τ_{rnn} tensor when a 96^3 grid is used, as can be observed in Figure 23. In the Figure, magnitudes from previous plots have been placed to enable a comparison. As can be seen in Fig. 23, although the most refined grid yields similar behaviour in first six seconds of simulation, the averaged magnitude of the surface tensor drops in subsequent stages even more rapidly than for 64^4 case. This could support the conclusion about the velocity field being less under-resolved on denser grids. Notwithstanding this facts, it has to be noted that [55] describes different tendency in the plots of (55) and of other τ_{rnn} components, that is, magnitudes of these ratios are increasing proportionally to the number of grid points.

An example of the interface shape obtained for $t = 7.6s$ using a 96^3 grid is presented in Figure 10, displaying a number of resolved film and "finger" formations. Additionally, simulation on a finest grid performed *without* the use of the ADM-τ model is presented in Figure 22, wich is to certain extent comparable with Figure 10. However, subsequent of the interface evolution even on this finest grid changes with the inclusion of ADM-τ model, as presented further in Figure 24.

We conclude by remarking that inclusion of τ_{rnn} force into the simulation of oil–water mixing case results in visible macroscopic differences (Figures 24 and 27) between obtained interfacial shapes. This is expected since τ_{rnn} ex-

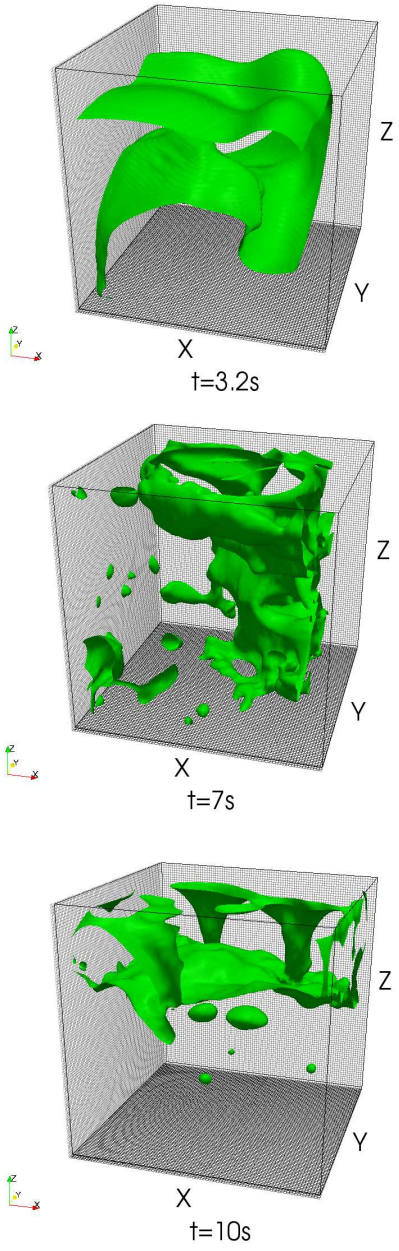

Figure 22: A 96^3 simulation - macroscopic evolution of the interface without the inclusion of τ_{rnn} tensor.

erts small, but constant influence on the interfacial geometry over entire simulation. Although overall mechanism of mixing with and without model usage is very similar, some ligaments, droplets and fluid "fingers" are either shifted in position or size, or not present at all. This difference can be observed in Fig. 24, in which the inclusion of τ_{rnn} is shown to have caused a shift in the bulk interface position and creation of more small-scale features. Overall assessment of this result - in other way than comparison with DNS *a priori* simulation would require experimental data, or DNS results of simulations using very fine discretisation to assure that simulation is fully resolved. Meanwhile

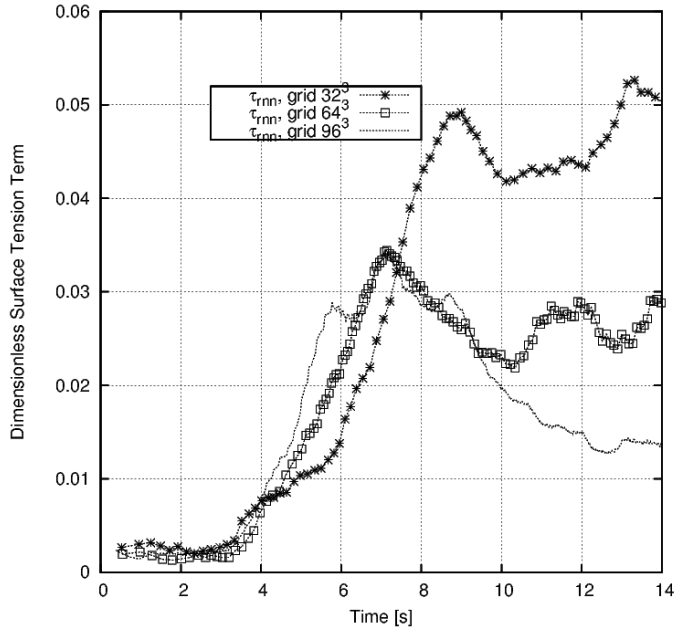

Figure 23: Average normalized magnitude of τ_{rnn} tensor and its components, non-dimensional, concerning the simulation on a 96^3 grid, plotted together with similar curves for 32^3 and 64^3.

authors of [55] conclude in their paper that for DNS to be resolved in this case, a grid of at least 128^3 is still not sufficient.

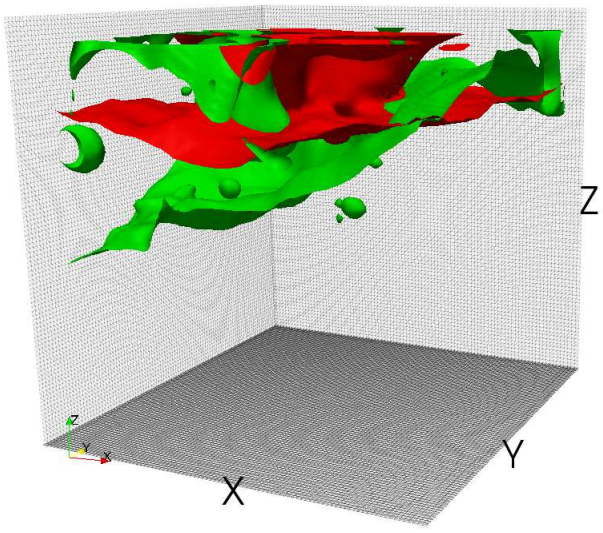

Figure 24: Simulation using the 96^3 grid with (green surface) and without (red) the inclusion of the τ_{rnn} tensor; $t \approx 11s$.

8.3. Further Assessment of τ_{rnn} Inclusion

As a means to assess the influence of the τ_{rnn} inclusion into the simulation, consider the case of a large droplet of heavy fluid in free fall, embedded in lighter fluid; similar to water droplet in air, although density ratio has been set to $\rho_w : \rho_a = 10 : 1$ for stability reasons. In Figure 25 the macroscopic, temporal evolution of such simulation, computed on a 64^3 grid, is presented.

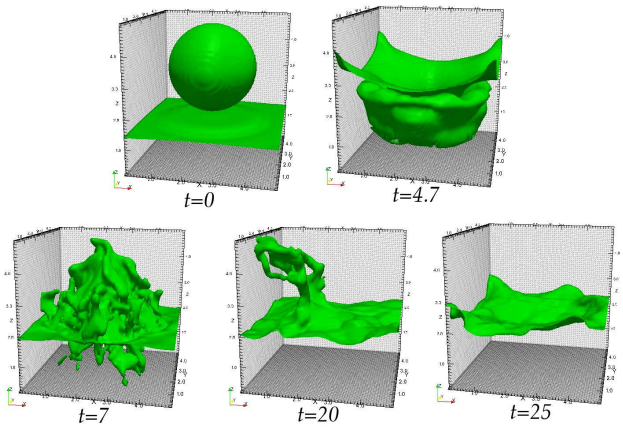

Figure 25: Macroscopic definition for the "splash case".

As it can be seen if Fig. 25, the droplet enters quiescent fluid mass after which a waving motion begins with bulk fluid mass oscillating in a way resembling a membrane (e.g. between $t = 4.7$ and $t = 7$ in Fig. 25). For $t = 7$ and $t = 20$, two of the uppermost positions of the oscillating mass are visible, when top wall of the domain is reached by it. Final image presented in Fig. 25 for $t = 25$ presents a more quiescent fluid surface.

For this particular simulated case, it is easy to observe that maximum values of τ_{rnn} tensor maxima is correlated with aforementioned "uppermost" positions of the oscillating mass, when surfacial area also has its peaks. This is easily observable in Figure 26, where the maxima have been plotted together with rescaled surface area of the interface. Virtually all of the peak values of $\tau_{rnn}|_z$ curve occur in $t \in [4, 12]$ and $t \in [16, 22]$ intervals, that correspond to "uppermost" positions of bulk mass during the first oscillations[15].

Such behavior of the tensor maxima suggests that τ_{rnn} tensor is not random, instead it is strongly dependent both on resolved interfacial shape and interfacial area. This could falsify any possible hypothesis saying that our results are merely a generation of a random vector field. Moreover, inspection of Figure 27 convinces us that the influence of tensor in equation (19) is significant – simulations with and without τ_{rnn} are divergent even in this preliminary stage, which is in accordance with conclusions of Vincent [55] that influence of this tensor will be significant even if no small-scale fluid formations are yet present. For the same simulation, a comparison of temporal realisations of approximated interfacial areas is shown in Fig. 28. Apart from the discernible difference in peak shapes

[15] We do not claim that the occurence of τ_{rnn} maxima implies high level of ratio (54). Maximum may occure locally - even in a single grid cell - and be traced to a specific interfacial formation as shown in Fig. 18.

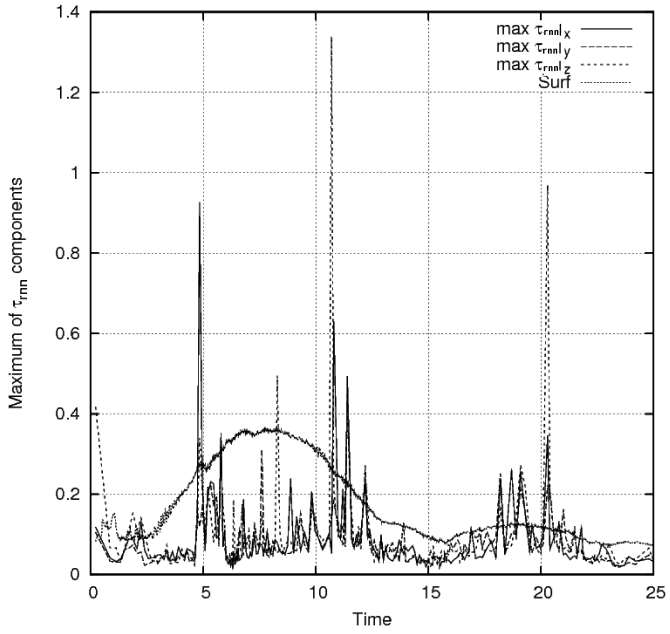

Figure 26: The τ_{rnn} tensor components maxima, plotted together with rescaled surfacial area for the splash case.

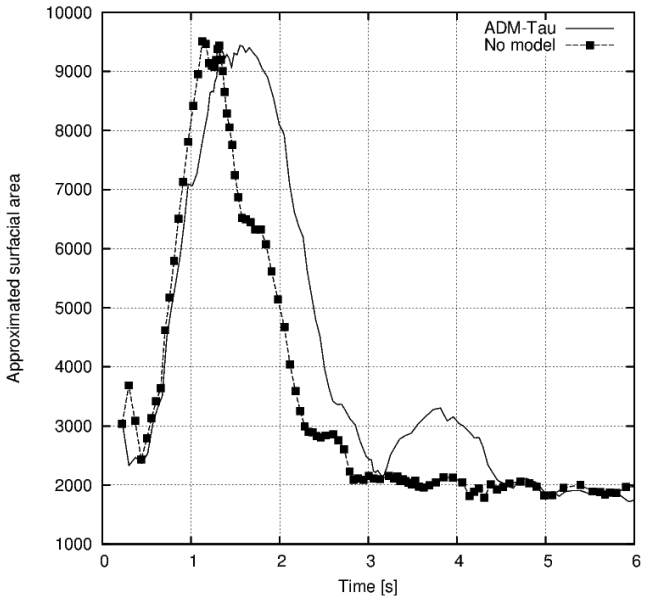

Figure 28: Approximated surfacial areas for simulations with (continuous line) and without the use of the ADM-τ model, for the splash case.

for $t \in [1, 2]$, an additional peak is visible in the simulation including ADM-τ model.

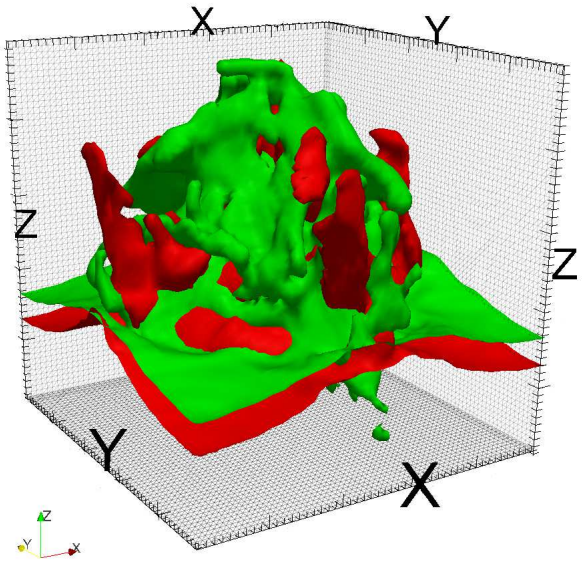

Figure 27: Comparison of the interface shapes in droplet splash simulation. Green surface corresponds to simulation including τ_{rnn} tensor. Red surface corresponds to simulation in which the tensor was omitted.

9. Discussion

We have presented and tested an approach of reconstructing sub-grid surface tension force in LES simulation, thus showing that introduction of one of LES-specific tensors emerging in two-phase flow is feasible with reasonable computational cost. Results of sample calculations indicate that values and behaviour of τ_{rnn} force are similar to DNS-based [55]. However, the "Sub-Grid Mass Transfer" (SMT) scalar term σ_1 discussed in Section 7 is not modelled yet, therefore we do not claim to have achieved a complete LES of two-phase flow. Technically, to cite Gorokhovski & Herrmann [25], the presented technique still has to be viewed as a *quasi-LES/DNS* simulation, since the SMT term is not modelled.

Evolution of τ_{rnn} sub-grid surface tension force term presented in this work is based on its definition, and rests more on a mathematically justified deconvolution of $\mathbf{u}^*$ by "inverted filtration" rather than being anyhow rooted in flow physics, e.g. by forming a relation between primitive variables and resulting τ_{rnn}. By this, we mean that ADM-based τ_{rnn} calculation is not a "model" *par excellence*, except in one sense: an assumption that $\mathbf{n}^* = \Psi(\mathbf{u}^*)$ operation described in Sect. 7 is a justified reconstruction of "deconvoluted curvature" κ^*. The latter quantity is meaningful in that τ_{rnn} is essentially a force created by the difference between resolved (filtered) and unresolved (subfilter) curvatures $\overline{\kappa}$ and κ. Present authors are however aware of potential drawbacks in presented model. For this reason, further studies could seem valuable in this field, such as:

- An ever more comprehensive parametric study of ADM-τ method to further prove its correctness with respect to DNS *a priori* calculations, similar to [33];
- Comparison of ADM-τ results with different possible approaches, such as direct reconstruction of $\mathbf{n}^*$ field

or κ^* deconvoluted curvature. Basing on methodology introduced in this article, the simplest method that yields correct results should be continuedly developed;

- Performing simulations for which more experimental data exist, such as using ADM-τ method for simulating atomization. Characteristics of those processes, like droplet distribution histograms, could be affected by τ_{rnn} force;
- Further work could also include modelling of σ_1 "subgrid mass transfer" tensor.
- Unlike direct reconstruction of $\mathbf{n}^*$ or κ^*, the ADM-τ scheme presented in this work is suitable for use with Domaradzki's reconstruction scheme [14] for $\mathbf{u}^*$. Hence calculations using it should constitute a good possibility for testing the method. Besides, in its original implementation, the Domaradzki scheme includes usage of dense grid, which could be very useful in calculating aforementioned "sub-grid mass transfer" tensor directly.

10. Finishing Remarks

The ADM-τ model has been tested and its results compared with *a priori* DNS results yielding satisfactory results, such as the temporal evolution of the ratio of norms of the ADM-reconstructed τ_{rnn} tensor and resolved inertia.

We believe this study should be followed by propositions of models for sub-grid mass transfer models, and assessments of the performance of ADM-τ model in other computational cases, at least to the extend permitted by availability of the DNS and experimental data.

11. Acknowledgements

Parts of this work were performed within the TIME-COP – AE (Toward Innovative Methods for Combustion Prediction in Aero-Engines) Project, co-funded by the European Commission within the Sixth Framework Program. Project no: AST5-CT-2006-030828.

The visualizations have been prepared using Mayavi [45], Paraview [19] and Gnuplot [62].

We would like to thank the anonymous reviewers of the article for valuable questions and suggestions.

List of Acronyms

- VOF - Volume of Fluid Method
- LS - Level Set Method
- LES - Large Eddy Simulation
- CLSVOF - Coupled Level Set-Volume of Fluid method
- DNS - Direct Numerical Simulation
- SMT - "Subgrid Mass Transport"
- GFM - Ghost Fluid Method
- SAILOR - Spectral and High Order Low Mach-Number LES (flow solver)
- ENO - Essentially Non-Oscillatory (differential scheme)
- WENO - Weighted Essentially Non-Oscillatory (differential scheme)
- PLIC - Piecewise Linear Interface Calculation
- ADM - Approximate Deconvolution Method

References

[1] S. Afkhami. *Phd Thesis*. Ph.d. thesis, University of Toronto, Toronto, 2007.
[2] A. Alajbegovic. LES formalism applied to multiphase flow. In *FEDSM2000*. Fluids Engineering Division Summer Meeting, May/June 2001.
[3] W. Aniszewski. *Large Eddy Simulation of Turbulent Two-Phase Flow*. Ph.D. thesis, Czestochowa University of Technology, Czestochowa, Poland, 2011.
[4] R. Aris. *Vectors, Tensors, and the Basic Equations of Fluid Dynamics*. Prentice Hall, Inc., 1962.
[5] G.K. Batchelor. *An Introduction to Fluid Dynamics*. Cambridge University Press, 1967.
[6] A. Berlemont. Coupling level set/ volume of fluid / ghost fluid methods: description and application on jet atomization. von karman lectures. (Lecture Notes), 2006.
[7] G. Bianchi et al. 3D large scale simulation of the high-speed liquid jet atomization. *SAE Technical Papers*, 2007.
[8] J. Brackbill et al. A continuum method for modeling surface tension. *JCP*, 100:335–354, 1992.
[9] A. Brandt. *Multigrid Techniques: 1984 guide with applications to fluid dynamics*. GMD-Studien 85, 1984.
[10] S. Cummins, M. Francois, and D. Kothe. Estimating curvature from volume fractions. *Computers and Structures*, 83:425–434, 2004.
[11] S. Dayal and S. Jain. A converse of taylors theorem on locally convex linear spaces. *Indian Journal of Pure and Applied Mathematics*, May 1985.
[12] E. de Villers et al. Large eddy simulation of primary diesel spray atomization. *SAE Technical Papers*, 2004.
[13] O. Desjardins and H. Pitsch. Detailed numerical investigation of turbulent atomization of liquid jets. *Atomization and Sprays*, 20(4):311–336, 2010.
[14] A. Domaradzki. An adaptive local deconvolution method for implicit LES. *JCP*, 213:413–436, 20062.
[15] J. Eaton and J. Fessler. Preferential concentration of particles by turbulence. *International Journal of Multiphase Flow*, 20:169–209, 1994.
[16] S. Elgobashi. Prediction of the particle-laden jet with a two-equation turbulence model. *Journal of Multiphase Flow*, 10:687–710, 1984.
[17] D. Enright et al. Animation and rendering of complex water surfaces. *ACM Trans Graph*, 21:736–44, 2002.
[18] D. Enright et al. A fast and accurate semi-lagrangian particle level set method. *Comput Struct*, 83:479–90, 2005.
[19] K. Moreland et al. Remote rendering for ultrascale data. *Journal of Physics: Conference Series*, 125, 2008.
[20] M. Sussman et al. A sharp interface method for incompressible two-phase flows. *Journal of Computational Physiscs*, 221:496–505, 2007.

[21] P. Trontin et al. Direct numerical simulation of a freely decaying turbulent interfacial flow. *International Journal of Multiphase Flow*, 36:891–907, 2010.
[22] R. Fedkiw et al. A non-oscillatory eulerian approach to interfaces in multimaterial flows (the ghost fluid method). *JCP*, 152:457–492, 1999.
[23] R. Fletcher. Conjugate gradient methods for indefinite systems. *Lecture Notes in Mathematics*, 506:773–789, 1976.
[24] B. Geurts and F. van der Bos. Numerically induced high-pass dynamics in large-eddy simulation. *Physics of Fluids 17*, 2005.
[25] M. Gorokhovski and M. Herrmann. Modeling primary atomization. *Annual Review of Fluid Dynamics*, 40:343–366, 2008.
[26] C. Hirth and B. Nichols. Volume of fluid (VOF) method for the dynamics of free boundaries. *Journal of Computational Physics*, 39:201–225, 1979.
[27] H. Jeanmart and G. Winckelmans. Investigation of eddy-viscosity models modified using discrete filters: A simplified âĂIJregularized variational multiscale modelâĂİ and an âĂIJenhanced field modelâĂİ. *Physics of Fluids*, 2007.
[28] I. Kataoka. Local instant formulation of two-phase flow. *Int.J.Multiphase Flow*, 12:745–758, 1986.
[29] M. Klein and J. Janicka. LES of primary breakup of film. In *ICLASS*, 2003.
[30] E. Labourasse, D. Lacanette, et al. Towards large eddy simulation of isothermal two-phase flows: Governing equations and *a priori* tests. *International Journal of Multiphase Flows*, 33:1–39, 2006.
[31] D. Lakehal et al. LES of bubbly turbulent shear flows. *Journal of Turbulence*, 3, 2002.
[32] P. Liovic & D. Lakehal. Interface-turbulence interactions and bubble dynamics. In *Seventh International Conference on CFD in the Minerals and Process Industries*. CSIRO, December 2009.
[33] J. Larocque, S. Vincent, et al. Parametric study of LES subgrid terms in a turbulent phase separation flow. *International Journal of Heat and Fluid Flow*, 31:536–544, 2010.
[34] F. Losasso, R. Fedkiw, and S. Osher. Spatially adaptive techniques for level set methods and incompressible flow. *Computers & Fluids*, 35:995–1010, 2006.
[35] R. Macer et al. A validated numerical simulation of diesel injector flow using a vof method. *SAE 2000-01-2932*, 2000.
[36] M. Marek, W. Aniszewski, and A. Boguslawski. Simplified volume of fluid method (SVOF) for two-phase flows. *TASK quaterly*, 12:255–265, 2008.
[37] M. Marek and A. Tyliszczak. Modeling of interaction of single droplet with turbulent flow. *Proceedings of Turbulence, Heat and Mass Transfer VI, Rome*, 2009.
[38] T. Ménard, S. Tanguy, and A. Berlemont. Coupling level set/ volume of fluid/ ghost fluid methods, validation and application to 3d simulation of the primary breakup of a liquid jet. *International Journal of Multiphase Flows*, 33:510–524, 2007.
[39] S. Osher and R. Fedkiw. *Level Set Methods and Dynamic Implicit Surfaces*. Springer-Verlag, 2003.
[40] B.J. Parker and D.L. Youngs. Two and three dimensional eulerian simulation of fluid flow with material interfaces.technical report 01/92. *UK Atomic Weapons Establishment, Aldermaston, Berkshire*, 1992.
[41] J. Pilliod and E. Puckett. Second order accurate volume of fluid algorithms for tracking material interfaces. *Journal of Computational Physics*, 1999:465–502, 2004.
[42] S. Pope. *Turbulent Flows*. Springer, 1996.
[43] S. Popinet. An accurate adaptive solver for surface-tension driven interfacial flows. *Journal of Computational Physics*, 228:5838–5866, September 2009.
[44] S. Zaleski R. Scardovelli. Analytical relations connecting linear interfaces and volume fractions in rectangular grids. *Journal of Computational Physics*, 164:228–237, 2000.
[45] P. Ramachandran and G. Varoquaux. Mayavi: 3D Visualization of Scientific Data. *Computing in Science & Engineering*, 13(2):40–51, 2011.
[46] R. Scardovelli and S. Zaleski. Direct numerical simulation of free-surface and interfacial flow. *Annu.Rev.Fluid Mech.*, 31:567–603, 1999.
[47] E. Shiriani. Turbulence models for flows with free surfaces and interfaces. *AIAA Journal*, 44:1454–1463, 2006.
[48] J. Smagorinsky. General circulation experiments with the primitive equations: I. the basic equations. *Mon. Weather Rev.*, 91:99–164, 1963.
[49] M. Stanislas, J. Jimenez, and I. Marusic. *Progress in wall turbulence: understanding and modelling. Proceeding of the WALLTURB International Workshop, Lille 2009*. Springer, 2010.
[50] S. Stolz, N. Adams, and L. Kleiser. An approximate deconvolution model for large-eddy simulation with application to incompressible wall-bounded flows. *Physics of Fluids*, april 2001.
[51] M. Sussman. A second order coupled level set and volume-of-fluid method for computing growth and collapse of vapor bubbles. *JCP*, 187:110–136, 2003.
[52] M. Sussman and M. Hussaini. A discontinuous spectral element method for the level set equation. *Journal of Scientific Computing*, 19:479–500, 2003.
[53] M. Sussman and E.G. Puckett. A coupled level set and volume-of-fluid method for computing 3d axisymmetric incompressible two-phase flows. *Journal of Computational Physiscs*, 162:301–337, 2000.
[54] S.Vincent. Private correspondence. , 2011.
[55] S.Vincent, J. Larocque, et al. Numerical simulation of phase separation and apriori two-phase LES filtering. *Computers and Fluids*, 37:898–906, 2008.
[56] G. Tomar et al. Numerical simulation of bubble growth in film boiling using CLSVOF method. *Physics of Fluids*, 17, 2005.
[57] G. Tomar et al. Multiscale simulations of primary atomization. *Computers and Fluids*, 39:1864–1874, 2010.
[58] A. Toutant, E. Labourasse, et al. Dns of the interaction between a deformable buoyant bubble and a spatially decaying turbulence: A priori tests for LES two-phase flow modelling. *Computers & Fluids*, 37:877–886, 2008.
[59] G. Tryggvason, R. Scardovelli, and S. Zaleski. *Direct Numerical Simulations of Gas-Liquid Multiphase Flows*. Cambridge Monographs, 2011.
[60] A. Tyliszczak and A. Boguslawski. LES of variable density bifurcating jets. *Complex Effects in Large Eddy Simulations, LNCSE*, 56:273–288, 2007.
[61] A. Tyliszczak, A. Boguslawski, and S. Drobniak. Quality of LES predictions of isothermal and hot round jet. *Quality and Reliability of Large Eddy Simulation, ERCOFTAC Series*, 12:259–270, 2008.
[62] Thomas Williams, Colin Kelley, and many others. Gnuplot 4.4: an interactive plotting program. `http://gnuplot.sourceforge.net/`, March 2010.
[63] F. Xiao et al. A simple algebraic interface capturing scheme using hyperbolic tangent function. *Int.J.Numer.Meth.Fluid*, 48:1023–1040, 2005.
[64] D. Youngs. Numerical simulation of turbulent mixing by rayleigh-taylor instability. *Fronts, Interfaces and Patterns*, page 32, 1984.